Journal of Sound and Vibration 637 (2026) 119805

Contents lists available at ScienceDirect

Journal of Sound and Vibration

journal homepage: www.elsevier.com/locate/jsvi

Prediction of potential interaction noise in a generic rotor–strut arrangement

R. Zamponi [a,b,*], A. Beni [a], A. Zarri [a], J. Christophe [a]

[a] von Karman Institute for Fluid Dynamics, Waterloosesteenweg 72, Sint-Genesius-Rode, B-1640, Belgium
[b] Delft University of Technology, Kluyverweg 1, Delft, 2629 HS, The Netherlands

ARTICLE INFO

Keywords:
Noise prediction
Potential interaction
Propeller noise
Conformal mapping
Unmanned aerial vehicles

ABSTRACT

The growing demand for quiet unmanned aerial vehicles (UAVs) calls for noise prediction tools capable of capturing the complex aerodynamic interactions occurring in rotor-airframe integrations at low computational cost. This paper presents an analytical framework to predict the potential-interaction tonal noise generated by a propeller operating upstream of its supporting strut, a dominant contributor to the acoustic signature of small UAVs. Aerodynamic sources of loading noise from the propeller and strut are modelled using potential-flow solutions, while a hypotrochoidal conformal mapping is employed to represent the inflow distortion induced by struts with arbitrary non-circular cross-sections. The method requires as input the spanwise distribution of steady loads from an isolated propeller, estimated through an unsteady panel solver that offers a favourable trade-off between computational efficiency and simulation fidelity. Analytical predictions are validated against experimental data for struts of varying cross-section diameters and shapes, different blade numbers, and multiple far-field observer locations. The results confirm that the models accurately capture the dominant physics of propeller-strut potential interaction, predicting sound pressure levels within 3 dB for most observer angles and blade-passing-frequency harmonics. The potential of the proposed methodology to support UAV noise optimisation is demonstrated by addressing the sound radiated by propellers with struts featuring spanwise-varying cross-sections.

1. Introduction

The rapid proliferation of small-size unmanned aerial vehicles (UAVs), particularly multicopters, has transformed both civilian and military operations owing to their agility, versatility, and low operating costs [1]. Their applications span agriculture, logistics, environmental monitoring, disaster response, public safety, surveillance, and defence, making them increasingly present in urban and rural environments [2]. However, this growth raises critical concerns about their noise emissions [3], which can adversely affect human health, community acceptance, and wildlife, while also compromising stealth in military applications. The design of low-noise UAVs is therefore essential, yet highly challenging, due to the intricate mechanisms involving aerodynamic sound generation and propagation [4]. Achieving this goal requires reliable prediction tools to be available throughout every stage of development, with analytical modelling being particularly valuable in the early-design phase, when the detailed geometry of the propulsion system is still unknown.

From a physical perspective, UAV noise arises primarily from rotor self-noise, linked to steady loads and thickness sources [5], and from complex interactions between rotors, interactions with the airframe, and non-uniformity in the upstream inflow, which induce flow distortions and thus unsteady loads on the propellers. These influences of the installation environment on the propulsion

* Corresponding author.
E-mail address: riccardo.zamponi@vki.ac.be (R. Zamponi).

https://doi.org/10.1016/j.jsv.2026.119805
Received 17 November 2025; Received in revised form 19 March 2026; Accepted 9 April 2026
Available online 14 April 2026

system, commonly referred to as aerodynamic installation effects [6], contribute to tonal components at the blade passing frequency (BPF) and its harmonics, as well as broadband noise [7,8]. Such sound sources are further affected by the low Mach and Reynolds numbers and the transitional flow regimes typical of UAV blade operation [9], which increase sensitivity to unsteady aerodynamic effects [10]. In addition, the presence of airframe components or other solid surfaces modifies the propagation and diffraction of UAV noise compared to free-field conditions, altering its acoustic footprint without affecting the actual sources, provided that no acoustic feedback loop occurs [11]. These influences are typically described as acoustic installation effects and fall outside the scope of the present study.

Among the various aerodynamic installation effects, a significant contribution to the noise radiated by a UAV arises from the potential interaction between the rotors and the downstream supporting struts owing to their close proximity in typical UAV architectures. Because the dominant physics of this interaction depend more on global parameters, such as strut cross-section and rotor-strut spacing, than on fine geometric details, it can be studied using simplified sub-systems, e.g. a propeller combined with a downstream cylinder. Following this approach, Zawodny and Boyd [12] performed experiments and numerical simulations to investigate rotor-airframe interaction noise in several propeller-cylinder arrangements under hovering conditions. Their analysis identified the cylinder as the dominant tonal noise source for higher BPF harmonics and out-of-plane observation angles, especially when positioned in close proximity to the propeller. These noise contributions were observed to decrease with increasing spacing and, more generally, to be highly sensitive to geometry, relative positioning with the rotor, and phase interference effects with the noise from the propellers. In contrast, broadband noise levels remained largely unchanged across configurations, indicating that this component was dominated by rotor self-noise. A similar experimental study on a propeller-cylinder configuration was conducted by Gojon et al. [13], who confirmed the dominant role of the strut in far-field noise radiation by systematically varying propeller blade numbers and the cylinder cross-section, size, and spacing relative to the rotor. For two-bladed propellers, steady aerodynamic performance and noise emitted at the BPF remained mostly unchanged, but higher-order BPF harmonics increased significantly, producing two distinct humps in the frequency spectrum. In the case of three- and four-bladed propellers, the presence of the cylinder had a non-negligible influence on thrust and torque, thus affecting the noise directivity pattern at the BPF. The database generated in this study was recently released as open source by Gojon and Jardin [14] and was used as a validation test case for the methodology proposed in the present research work. The conclusions of Gojon et al. [13] were corroborated by the numerical study of Doué et al. [15], which showed that the BPF harmonic amplitudes corresponding to the first of the two frequency humps observed experimentally were produced by the cylindrical strut. At higher BPF harmonics, the noise source was concentrated in the strut region beneath the propeller blade tip, indicating a noise generation mechanism associated with tip vortex impingement.

Several researchers have attempted to analytically model propeller-strut potential interaction noise in the past decade. Using a hybrid analytical-numerical approach, Roger and Kucukcoskun [16] investigated the sound predictions in the early-stage design of a helicopter tail-rotor architecture. The study focused on the interaction of the rotor with stationary vanes or supporting struts, making use of simplified linearised unsteady aerodynamic theories to determine the lift fluctuations acting as sound sources on the rotor blades. Despite approximations in flow distortion modelling, which was based on the two-dimensional potential flow around a circle, the analytical formulations yielded predictions considered reasonably accurate for preliminary design studies or noise impact assessments. The same approach was later followed by Roger and Moreau [17] to model the potential flow distortion around the struts, treated as circular cylinders, in quadcopter rotors. In this work, the authors developed analytical tools capable of providing fast and reliable predictions for varying input parameters, such as rotor-strut distance and blade number. Roger et al. [4] proposed a methodology to predict the loading noise generated by rotor blades interacting with the potential field of a cylindrical strut, which was formulated as a diffraction problem, i.e. including acoustic installation effects. In this case, the presence of the strut was modelled using scattering theory and a Green's function tailored to a rigid cylindrical geometry [18]. The low-frequency amplification of rotor noise due to cylinder scattering was qualitatively reproduced. This study was later extended by Rendón-Arredondo et al. [19], who performed high-fidelity simulations to investigate how propeller-strut spacing affects both the flow field and the resulting acoustic signature. The simulation data were then used as input to the analytical model of Roger et al. [4], yielding better agreement with the measurements than that achieved using the analytical approach alone. Wu et al. [20] developed two uncoupled methods to describe the unsteady loading noise radiated from the propeller and the strut in a rotor-cylinder configuration. The first method was based on the work of Parry and Crighton [21], which addressed the interaction of an aerofoil with the potential field generated by a periodic array of downstream elliptical cylinders, while the second method relied on a description of the flow field by means of complex potential theory. The authors reported a reasonable agreement between the analytical calculations and the experimental data. Vella et al. [22] employed a similar two-dimensional framework to predict the potential noise generated due to the propeller-cylinder interaction in one of the experimental configurations of Gojon et al. [13]. Interestingly, their models correctly reproduced the envelope of the first frequency hump associated with cylinder radiation and the directivity patterns of several BPF harmonics. Likewise, Rendón-Arredondo et al. [23] applied the same methodology to calculate the unsteady loads and noise for a similar rotor-strut configuration, which showed good agreement with high-fidelity simulations and experimental data. Although they slightly overpredicted propeller noise at the BPF due to unmodelled three-dimensional effects and flow regime changes near stall, the models reproduced overall noise levels, spectra, and directivity patterns, confirming the usefulness of such methods despite the strict underlying assumptions.

Most of the prediction tools discussed above require experimental or high-fidelity numerical data as input for the models, particularly for spanwise loading distributions on the propeller and induced velocities. Low-fidelity approaches, such as blade element momentum theory (BEMT), are considered less reliable due to their sensitivity to low-Reynolds-number effects on the propeller blades and their limited ability to accurately capture blade-tip phenomena, resulting in significant uncertainties [4]. This limitation reduces the applicability of analytical methods, especially in cases where high-fidelity simulations or experimental data are unavailable. In this research work, we propose an alternative approach, making use of a fast mid-fidelity simulation framework to generate the aero-

dynamic data needed for mathematical modelling. It is important to emphasise that only data associated with an isolated propeller need to be simulated, as the unsteady aerodynamic effects induced by the presence of the strut are modelled analytically.

Furthermore, the methodology proposed in the aforementioned piece of literature was developed only for struts assimilated to straight circular cylinders, which are mathematically easier to handle. However, in practical applications, supporting struts often feature non-circular cross-sections, tapered geometries, or aerofoil-like profiles designed to reduce drag and noise. Such realistic geometries introduce potential distortions that cannot be accurately captured by the simplifying assumption of a circular cylinder of constant cross-section. For instance, both Zawodny and Boyd [12] and Kim et al. [24] investigated the effect of conical struts placed in proximity to a propeller on tonal noise radiation and concluded that variations in spanwise cross-sections can be associated with increased efficiency of sound generation compared to straight cylindrical geometries.

A recent attempt to extend analytical predictions beyond circular cylinders was presented by He et al. [25], who adapted the method of Parry and Crighton [21] to evaluate the potential-interaction tones generated by a rotor operating upstream of aerofoil-shaped struts in multi-rotor UAVs. The struts were modelled as simplified lifting surfaces subjected to potential-flow disturbances, and the resulting noise predictions showed reasonable agreement with both numerical simulations and experimental measurements. However, their formulation remains limited to aerofoil geometries and does not generalise to arbitrary strut shapes. A comprehensive analytical prediction approach applicable to generic rotor-strut configurations is thus needed but remains lacking. In addition to assessing the suitability of mid-fidelity methods for generating accurate inputs to noise prediction models, our paper aims to address this gap by proposing a methodology to model potential interaction noise in generic rotor-strut arrangements. We pursue this objective using conformal mapping techniques, which enable the analysis of potential flows past bluff bodies of nearly arbitrary shape [26].

The remainder of the document is structured as follows. The analytical models describing the various noise generation mechanisms in a generic rotor-strut configuration, together with the mapping approach, are presented in Section 2. The measurement setup used to validate the methodology, along with the mid-fidelity simulation framework proposed to calculate the aerodynamic inputs, is described in Section 3. In Section 4, the main results are outlined and discussed, including the application of the proposed methodology to struts with non-circular and spanwise-varying cross-sections. Finally, conclusions are drawn in Section 5.

2. Theory

This section aims to provide a description of the noise generated in a propeller-strut arrangement with minimal mathematical effort. As introduced in Section 1, several aeroacoustic mechanisms contribute to the overall sound radiation in this configuration. Thickness noise originates from the displacement of air by the rotating blades, with its intensity strongly influenced by the blade thickness. Blade loading noise arises from the aerodynamic loads acting on the blades, which can be steady, i.e. driven by the overall aerodynamic properties of the rotor such as thrust and torque, or unsteady, i.e. resulting from flow non-uniformities across the rotor disc, like the potential flow distortion introduced by the presence of a downstream strut [27]. Additional strong noise sources are also distributed on the strut as a result of time-varying aerodynamic potential interactions, including blade circulation effects and the impact of wake or tip vortices on the strut [22]. As this component is stationary, steady loads or thickness do not contribute to noise radiation, and the radiated sound pressure originates only from unsteady loading sources.

In the analytical formulation that follows, we model separately the sources of aerodynamic noise and the sound propagating from these sources, adopting the classical framework of acoustic analogies [5]. The emphasis here is on the tonal noise contributions, which are deterministic in essence. Several assumptions are required for mathematical tractability: (i) both blade and strut are considered unswept, acoustically compact in the chordwise direction, and subject to a low-reduced-frequency approximation for the unsteady aerodynamic response, which limits the frequency range of applicability of the proposed methodology; (ii) the observer is located in the geometric far-field and is defined according to the spherical coordinate system shown in Fig. 1, with R, Θ, and Φ being the radial distance, polar angle, and azimuthal angle, respectively; (iii) the radial loads on the blade and the strut are deemed negligible; (iv) the flow distortions induced by the presence of the strut are described as small disturbances superimposed on an axisymmetrically-uniform base flow, and fluctuations in the aerodynamic forces are assumed to be small compared to the steady loads.

2.1. Blade loading noise

The loading noise generated by a propeller operating in a stationary distortion is radiated at multiples of the BPF, which is defined as $mB\Omega/(2\pi)$, with B being the number of blades and Ω the rotational speed. In the geometric far-field, the complex-valued sound-pressure amplitude computed at the observer location $\mathbf{x}$ and at the mth harmonic of the BPF, with the standard negative exponential time convention $\mathrm{e}^{-\mathrm{i}2\pi f t}$ for monochromatic waves, reads [28]

$$p_{mB}(\mathbf{x}) = -\frac{\mathrm{i}k_{mB}B\mathrm{e}^{-\mathrm{i}k_{mB}R}}{4\pi R}\sum_{s=-\infty}^{\infty}\mathrm{e}^{\mathrm{i}(mB-s)(\Phi-\pi/2)}\times\int_{r_{\mathrm{root}}}^{r_{\mathrm{tip}}}J_{mB-s}\left(k_{mB}r\sin\Theta\right)\left[\frac{mB-s}{k_{mB}r}F_{b,\phi}^{(s)}(r)+\cos\Theta F_{b,z}^{(s)}(r)\right]\mathrm{d}r, \tag{1}$$

where c_0 is the speed of sound, J_n is the Bessel function of the first kind of order n, and $k_{mB} = mB\Omega/c_0$ is the wavenumber related to the mth BPF harmonic. $F_{b,\phi}^{(s)}$ and $F_{b,z}^{(s)}$ are the tangential and axial blade loading harmonics, respectively, and represent the complex-valued coefficients of the Fourier series of the periodic forces per unit span acting on the blade element of radius r from the rotor axis. The steady components of these loading distributions, corresponding to the $s = 0$ harmonic, comprise the mean aerodynamic loads produced by the propeller. Owing to the assumptions of aerodynamic compactness and zero sweep, the blade can be described by a single azimuthal location, and the integration is carried out only along the radial direction, which is compatible with a strip-theory approach to rotor noise.

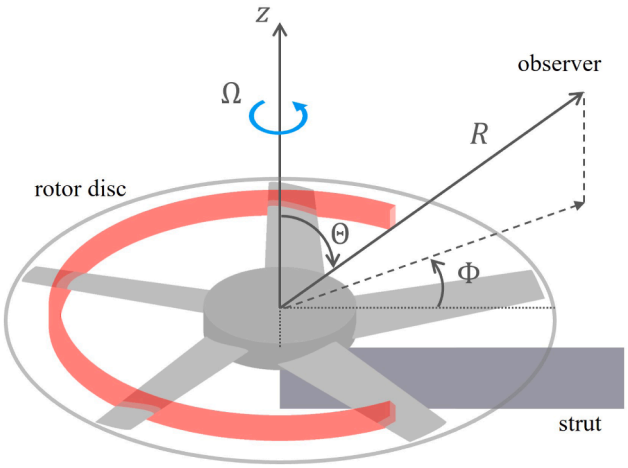

Fig. 1. Reference system definition for the propeller-strut setup. In red an annular strip at the generic radius r. (For interpretation of the references to colour in this figure legend, the reader is referred to the web version of this article.)

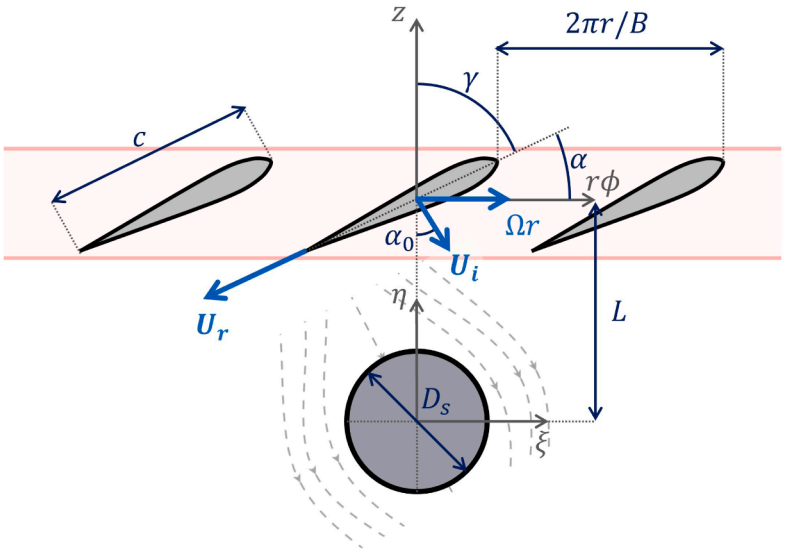

Fig. 2. Two-dimensional unwrapped representation of the annular strip of arbitrary radius in Fig. 1 expressed in a Cartesian reference frame. The strut is assimilated to a cylinder of circular cross-section subjected to the velocity induced by an infinite sum of blade passages.

Eq. (1) states that the acoustic pressure p_{mB} can only be predicted once the blade loading harmonics are known as source terms, which is a matter of aerodynamics. In a rotor-strut configuration, $F_{b,\phi}^{(s)}$ and $F_{b,z}^{(s)}$ are generated by the mean-flow distortion induced by the downstream strut. A simple two-dimensional analytical model to calculate this distortion was proposed by Roger et al. [29] and is based on the classical incompressible solution for the potential flow around a circle. The present work builds upon that model and aims to generalise it to struts of arbitrary shapes in Section 2.4.

Fig. 2 shows an unwrapped representation of an annular strip of radius r in the propeller-strut arrangement depicted in Fig. 1. The propeller blade sections, which are separated by $2\pi r/B$ and are assimilated to flat plates due to the small blade thicknesses, translate past a cylindrical strut of circular cross-section with a velocity Ωr. Each blade features a chord c and is placed at a pitch angle α corresponding to a stagger angle γ with respect to the rotor axis, while D_s is the strut diameter. The mid-chords of the blades lie at a distance of L from the centre of the circular cross-section. The strut is immersed in the airflow induced by the propeller $\boldsymbol{U}_i$, which comprises an axial component, i.e. the downwash, and a tangential component, i.e. the swirl, with α_0 denoting the flow swirl angle defined according to Fig. 2. These quantities are evaluated at the level of the rotor disc as if the propeller were isolated, which implies that possible variations in the induced velocities due to the presence of the strut are neglected, consistently with a no-coupling assumption [22]. Moreover, the flow acceleration downstream of the propeller due to the slipstream contraction is here ignored, allowing $\boldsymbol{U}_i$ to be considered uniform throughout the unwrapped two-dimensional domain. In the following derivations, we will omit the radial dependence of c, α, γ, U_i, and α_0 for the sake of clarity.

The flow distortion on the rotor disc caused by the strut can be analysed by solving the equivalent two-dimensional incompressible potential flow problem. We introduce the complex potential function $f(\zeta)$, which depends on the complex variable $\zeta = \xi + \mathrm{i}\eta$. Here, ξ and η represent the Cartesian coordinates in the two-dimensional flow plane centred on the strut, as shown in Fig. 2. According to the Milne-Thomson circle theorem, the complex potential produced by a cylinder in a uniform free stream reads [30]

$$f(\zeta) = \mathrm{i}U_i\left(\zeta \mathrm{e}^{-\mathrm{i}\alpha_0} - \frac{D_s^2}{4\zeta}\mathrm{e}^{\mathrm{i}\alpha_0}\right), \tag{2}$$

where $U_i = |\boldsymbol{U}_i|$. The flow velocities in the ξ- and η-directions can then be computed by $u(\zeta) = \Re\{\partial f/\partial\zeta\}$ and $v(\zeta) = -\Im\{\partial f/\partial\zeta\}$, respectively. The blade segments experience these velocity components as an upwash, which is defined as the projection of the velocity disturbance normal to the chord. Considering that $\xi = r\phi$ and $\eta = L$ on the rotor disc, the upwash disturbance at radius r is

$$w(r,\phi) = -\left[u(r,\phi) - U_i \sin\alpha_0\right]\sin\alpha + \left[v(r,\phi) - U_i\cos\alpha_0\right]\cos\alpha. \tag{3}$$

An interesting point to make is that the two-dimensional nature of this model offers an advantage when dealing with struts of non-uniform cross-section and varying distances from the propeller. In this regard, both D_s and L can be thought of as functions of the radius r. We will address this point in Section 4.3.

Although w is stationary, the blade experiences a periodic azimuthal distortion in its reference frame. Consequently, the sth harmonic of the upwash disturbance can be obtained through a Fourier series expansion:

$$w_s(r) = \frac{1}{2\pi}\int_0^{2\pi} w(r,\phi)\mathrm{e}^{\mathrm{i}s\phi}\,\mathrm{d}\phi, \quad s \geq 1. \tag{4}$$

Each distortion harmonic w_s excites the blade loading harmonic of the same order through an unsteady aerodynamic transfer function. Under the assumption of aerodynamically compact blade chords, i.e. we neglect chordwise phase variations in the unsteady loads, this lift function can be obtained from Sears' theory [31]. A formulation of the unsteady lift response for the case of a rotor cascade interacting with the potential field produced by a stator cascade was derived by Kemp and Sears [32] and reads

$$K(\sigma,\mu) = C(\sigma)\left[J_0(\mu) - \mathrm{i}J_1(\mu)\right] + \frac{\mathrm{i}\sigma}{\mu}J_1(\mu), \tag{5}$$

with

$$\sigma = \frac{s\Omega c}{2U_r}, \qquad \mu = \frac{\mathrm{i}sc}{2r}\mathrm{e}^{-\mathrm{i}\gamma},$$

and C being the Theodorsen function [33]. Here, U_r is the projection of the relative velocity seen by the blade section (see Fig. 2), which is given by

$$U_r(r) = \sqrt{\left(\Omega r - U_i\sin\alpha_0\right)^2 + \left(U_i\cos\alpha_0\right)^2}, \tag{6}$$

on the chord line. An approach based on Sears' model indeed requires that the incoming mean velocity be aligned with the chord and that the disturbance vector of the velocity, i.e. the upwash w, be normal to it. In practical applications, the propeller blades typically operate at non-zero averaged angles of attack, making the projection of the relative velocity necessary to define an equivalent Sears' problem.

The harmonics of the unsteady lift per unit span are subsequently derived as

$$L_s(r) = \pi\rho_0 c U_r(r) w_s(r) K^*, \tag{7}$$

where ρ_0 is the fluid density, * denotes the complex conjugate, which is required according to the adopted convention $\mathrm{e}^{-\mathrm{i}2\pi f t}$ for monochromatic waves, and the lift harmonics associated with negative s are computed as $L_{-s} = L_s^*$. Finally, L_s can now be decomposed into the axial and tangential loading distributions in Eq. (1) following

$$F_{b,\phi}^{(s)}(r) = L_s(r)\cos\gamma, \qquad F_{b,z}^{(s)}(r) = -L_s(r)\sin\gamma. \tag{8}$$

2.2. Blade thickness noise

For thin unswept propeller blades featuring acoustically compact chords, we can express the complex-valued sound-pressure amplitude computed in the geometric far-field at the mth harmonic of the BPF due to the air volume displaced by the motion of the blade as [28]

$$p_{mB}(\mathbf{x}) = -\frac{mk_{mB}B^2\rho_0 c_0\Omega\mathrm{e}^{-\mathrm{i}k_{mB}R}}{4\pi R}\mathrm{e}^{\mathrm{i}mB(\Phi-\pi/2)} \times \int_{r_{\mathrm{root}}}^{r_{\mathrm{tip}}} J_{mB}\left(k_{mB}r\sin\Theta\right)\Delta h c^2\,\mathrm{d}r. \tag{9}$$

Here, Δh denotes a representative thickness of the blade section, expressed per unit chord length [27]. For compact blade chords, the maximum normalised thickness t/c provides an adequate approximation. This formulation highlights how the thickness contributes to the source strength, and the result is independent of the blade angle of attack or camber. Unlike rotor loading noise, the thickness source strength is defined exactly by the blade geometry, making its evaluation more straightforward.

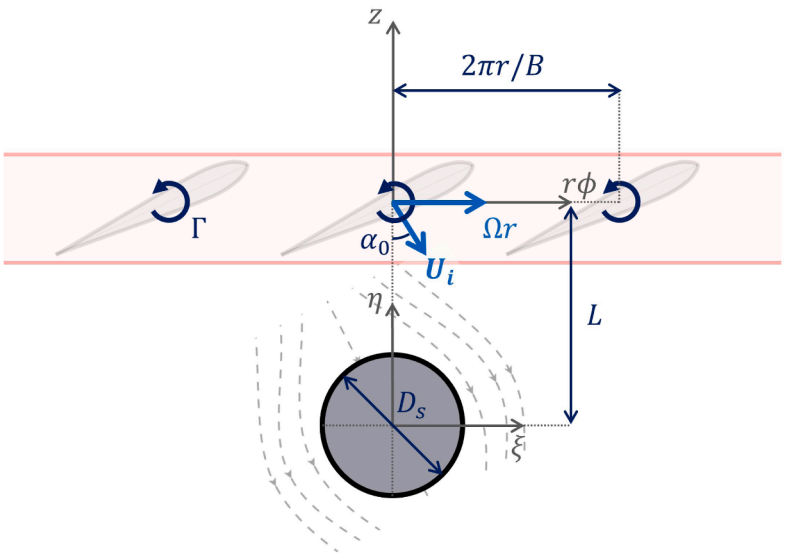

Fig. 3. Schematic of the equivalent two-dimensional incompressible potential problem associated with the unwrapped representation in Fig. 2. The blade sections are replaced by point vortices located at the mid-chord and characterised by a circulation Γ.

2.3. Strut loading noise

As mentioned above, the propeller-strut potential interaction also includes sources of loading noise distributed on the strut surface. At short separation distances, the unsteady loads on this component are dominated by the potential field induced by the nearby passing blades [20]. The method used to describe this noise source is analogous to that adopted for modelling propeller-radiated sound and is based on the prediction of rotor-stator noise proposed by Hanson [34]. The idea is to assimilate the strut to a stator with one non-profiled vane. The resulting expression for the complex-valued sound-pressure amplitude at the mth harmonic of the BPF for an observer in the geometric far-field reads

$$p_m(\mathbf{x}) = -\frac{\mathrm{i}k_{mB}\mathrm{e}^{-\mathrm{i}k_{mB}R}}{4\pi R}\sum_{s=-\infty}^{\infty}\mathrm{e}^{\mathrm{i}(mB-s)(\Phi-\pi/2)}\times\int_{r_{\mathrm{root}}}^{r_{\mathrm{tip}}}J_{mB-s}\left(k_{mB}r\sin\Theta\right)\left[\frac{mB-s}{k_{mB}r}F_{s,\phi}^{(m)}(r)+\cos\Theta F_{s,z}^{(m)}(r)\right]\mathrm{d}r. \tag{10}$$

What distinguishes Eq. (10) from Eq. (1) is that only one loading harmonic contributes to each sound harmonic m, since the strut is stationary [22]. The remaining terms in the two formulations are almost identical, including the Bessel functions, which implies that strut and blade loading noise are emitted at the same frequencies and exhibit a similar radiation efficiency of the source terms. As in the previous cases, the integration is performed solely along the radial direction.

The noise prediction problem reduces once again to finding a suitable modelling framework for the tangential and axial loads acting on the strut. A simple approach based on the incompressible potential flow problem around a two-dimensional circular cylinder was recently formulated by Wu et al. [20] and subsequently employed by Vella et al. [22]. We will extend this analytical model to accommodate struts of nearly-arbitrary shapes in Section 2.4.

A schematic of the equivalent potential flow problem is depicted in Fig. 3. The principle is to assimilate the lifting blade cross-section to a point vortex located at the mid-chord, placed successively at various horizontal positions relative to the strut cross-section to simulate the blade passage. At each radial position, the point vortex carries a circulation Γ, defined as positive for counter-clockwise rotation (see Fig. 1), and related to the lift per unit span acting on the local blade section. It is important to note that the choice of placing the point vortex at the blade mid-chord, although consistent with previous literature [22], is arbitrary and may introduce uncertainty in the estimation of the relative distance between the vortex and the strut, affecting the unsteady loads imparted on the latter. A more realistic approach to the problem would be to model the blade section as a vortex line distributed along the chord, which will be addressed in future work.

For the aerodynamic rotor-stator problem defined by the lift function in Eq. (7), a formulation for the quasi-steady circulation that accounts for the azimuthal periodicity of the flow distortion in the propeller reference frame, and hence for the unsteady effects linked to the propeller-strut coupling, reads [32]

$$\Gamma(r,\phi) = \Gamma_0 + \sum_{\substack{s=-\infty\\ s\neq 0}}^{\infty}\pi c w_s(r)\mathrm{e}^{-\mathrm{i}s\phi}\left[J_0(\mu)-\mathrm{i}J_1(\mu)\right]^*, \tag{11}$$

where $\Gamma_0 = \overline{L}/(\rho_0 U_r)$ is the circulation associated with the steady lift force per unit span $\overline{L}$ through the Kutta-Joukowski theorem, which provides the greatest contribution to Γ.

We can now modify the flow potential in Eq. (2) to include the contribution of the point vortex representing the blade passage and its image according to the Milne-Thomson circle theorem [35]:

$$f(\zeta) = \mathrm{i}U_i\left(\zeta \mathrm{e}^{-\mathrm{i}\alpha_0} - \frac{D_s^2}{4\zeta}\mathrm{e}^{\mathrm{i}\alpha_0}\right) - \frac{\mathrm{i}\Gamma}{2\pi}\log\left(\zeta - \zeta_v\right) + \frac{\mathrm{i}\Gamma}{2\pi}\log\left(\frac{D_s^2}{4\zeta} - \zeta_v^*\right), \tag{12}$$

where $\zeta_v = \xi_v + \mathrm{i}\eta_v$ denotes the complex coordinate of the point vortex translating in the positive ξ-direction at the level of the rotor disc, i.e. $\xi_v = \Omega r t$ and $\eta_v = L$. The unsteady Bernoulli principle allows the fluid pressure p to be determined from the flow potential according to

$$p(\zeta) + \frac{1}{2}\rho_0 U(\zeta)^2 + \rho_0\frac{\partial\varphi}{\partial t} = \text{constant}, \tag{13}$$

where $U(\zeta)^2 = u(\zeta)^2 + v(\zeta)^2 = |\mathrm{d}f(\zeta)/\mathrm{d}\zeta|^2$ and $\varphi = \Re\{f(\zeta)\}$, with the latter representing the velocity potential. The constant on the right-hand side of Eq. (13) can be calculated by considering a point at $|\zeta| \to \infty$, yielding

$$p \to p_\infty, \qquad U^2 \to U_i^2, \qquad \frac{\partial\varphi}{\partial t} \to \Re\left\{\frac{\mathrm{i}\Gamma\Omega r}{2\pi\zeta_v^*}\right\}, \tag{14}$$

p_∞ being the static pressure of the fluid. The pressure p is defined throughout the fluid domain, including on the strut surface, which is parametrised using the azimuthal angle θ_s as $\zeta_s = D_s\mathrm{e}^{\mathrm{i}\theta_s}/2$. In light of the above, the relative pressure extracted on the strut reads [20]

$$p(\zeta_s) - p_\infty = \frac{1}{2}\rho_0\left[U_i^2 - U(\zeta_s)^2\right] + \rho_0\frac{\Gamma\Omega r}{2\pi}\Re\left\{\frac{\mathrm{i}}{\zeta_v^*} + \frac{\mathrm{i}}{\zeta_v - \zeta_s} - \frac{\mathrm{i}}{\zeta_v^* - \frac{D_s^2}{4\zeta_s}}\right\}. \tag{15}$$

This formulation considers a single blade passage. In practice, the propeller blades pass over the strut at periodic intervals of $T_b = 2\pi/(B\Omega)$, which, in the corresponding two-dimensional potential flow problem, is equivalent to considering an infinite cascade of point vortices translating along the ξ-direction, spaced $2\pi r/B$ apart (see Fig. 3). We account for this effect by summing the contributions of n vortices with complex coordinates $\zeta_v\left(t + T_b n\right)$ in Eqs. (12) and (15), with n ranging from $-\infty$ to ∞.

Eq. (15) can now be integrated over the strut surface to retrieve the total tangential and axial forces per unit span exerted on this component:

$$F_{s,\phi}(r,t) = -\frac{D_s}{2}\int_0^{2\pi} p(\zeta_s)\cos\theta_s\,\mathrm{d}\theta_s, \quad F_{s,z}(r,t) = -\frac{D_s}{2}\int_0^{2\pi} p(\zeta_s)\sin\theta_s\,\mathrm{d}\theta_s, \tag{16}$$

which can be expanded in Fourier series because of their periodic nature. The corresponding sth harmonics read

$$F_{s,\phi}^{(s)}(r) = \frac{1}{T_b}\int_0^{T_b} F_{s,\phi}(r,t)\mathrm{e}^{\mathrm{i}sB\Omega t}\,\mathrm{d}t, \quad F_{s,z}^{(s)}(r) = \frac{1}{T_b}\int_0^{T_b} F_{s,z}(r,t)\mathrm{e}^{\mathrm{i}sB\Omega t}\,\mathrm{d}t \tag{17}$$

and are used in Eq. (10) to predict the acoustic pressure radiated by the strut. It should be noted that the potential flow past a cylinder does not accurately represent the flow in the aft portion of the strut, where separation is likely to occur. This may affect the outcome of the integration in Eq. (16). Nevertheless, it can be argued that the surface pressure contributing most to the force estimation originates from the front region, which is exposed to the effect of the blade passage, so deviations in the aft section are not expected to significantly impact the integration results.

2.4. Conformal mapping

The two-dimensional potential flow models implemented in Sections 2.1 and 2.3 have been formulated for a strut characterised by a circular cross-section. Starting from these analytical solutions, we can address the problem of computing the potential flow around a generic polygonal-shaped cylinder, closer to a realistic strut, using the conformal mapping technique. In particular, a conformal transformation makes it possible to relate the simple circular boundary in the reference ζ-plane to a polygonal boundary in the physical plane. Since Laplace's equation governing the potential flow is invariant under conformal transformations, the known solution for the circular cylinder can be mapped back into the physical plane owing to the superposition principle of potential flow, thus capturing the influence of the effective strut geometry on the flow field.

In the present study, we employ a hypotrochoidal mapping function to recreate various polygonal geometries with finite radii at the corners, following the approach of Solanki and Sharma [36]. A hypotrochoid is a type of cycloidal curve traced by a point located at an offset distance ρ from the centre of a circle of radius R_r as it rolls without sliding inside a fixed circle of radius R_d (see Fig. 4 for the example of a square cross-section cylinder). It is defined by the parametric equations

$$\begin{cases} x_t(\theta_s) = (R_d - R_r)\cos\left(\theta_s + \theta_0\right) + \rho\cos\left(\dfrac{R_d - R_r}{R_r}\theta_s - \theta_0\right) \\ y_t(\theta_s) = (R_d - R_r)\sin\left(\theta_s + \theta_0\right) - \rho\sin\left(\dfrac{R_d - R_r}{R_r}\theta_s - \theta_0\right), \end{cases} \tag{18}$$

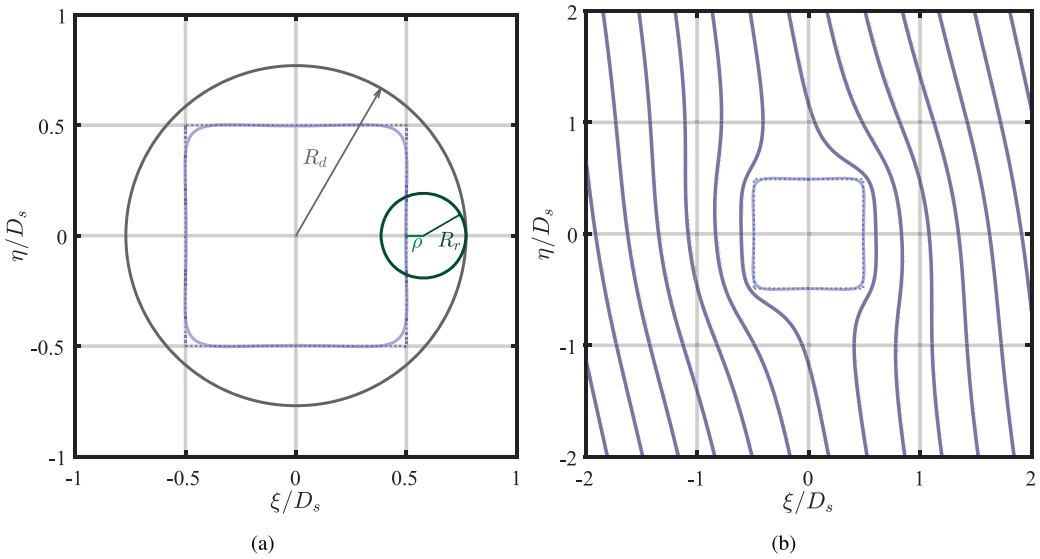

Fig. 4. (a) Schematic of the hypotrochoid used to generate a square cross-section cylinder and (b) corresponding potential flow field for a free stream at $\alpha_0 = \pi/18$. The dashed lines indicate the reference prescribed geometry, while the solid lines show the resulting hypotrochoidal curve. Input parameters for the hypotrochoid are listed in Table A.1.

where θ_0 allows for the rotation of the polygonal-shaped cylinder from the positive real axis. The corresponding mapping function reads

$$Z(\zeta) = R_d\left[\left(1-\frac{1}{N}\right)\zeta + \frac{\rho}{R_d}\frac{1}{\zeta^{N-1}}\right]e^{i\theta_0}, \tag{19}$$

where $N = R_d/R_r$ and the complex coordinate ζ is defined outside the hypotrochoid. For a closed curve, N should be an integer number greater than 2. ρ ranges from 0 to R_r and determines the radius of the corners and the straightness of the polygonal sides.

We calculate the resulting complex flow velocity by differentiating the potential function f derived from Eqs. (2) and (12) with respect to the hypotrochoidal mapping function defined in Eq. (19). Applying the chain rule gives

$$f'(Z) = u(Z) - iv(Z) = R_d\left(1-\frac{1}{N}\right)\frac{\partial f(Z)}{\partial \zeta}\zeta'(Z), \tag{20}$$

where $\zeta' = d\zeta/dZ$. Here, the multiplicative term $R_d(1-1/N)$ compensates for the scaling introduced by the mapping, as follows from Eq. (19) in the limit $\rho \to 0$ [36]. The velocity components in the ξ- and η-directions can then easily be derived from the real and imaginary parts of the right-hand side of Eq. (20), respectively, and used to compute the upwash experienced by the propeller blade in Eq. (3) and the velocity magnitude U in Eq. (15). This approach preserves the applicability of the Milne-Thomson circle theorem to the flow potential f since the construction is carried out in the ζ-plane before mapping to the physical one.

Furthermore, the term involving $\partial\varphi/\partial t$ in Eq. (15) is unaffected by conformal mapping because the map is time-independent. Owing to the coordinate invariance of the unsteady Bernoulli equation, and to the fact that the constant value of $\partial f/\partial t$ as $\zeta \to \infty$ is unchanged with respect to the circular cross-section case, the relative pressure on the mapped strut surface $Z_s = Z(\zeta_s)$ reads

$$p(Z_s) - p_\infty = \frac{1}{2}\rho_0\left[U_i^2 - U(Z_s)^2\right] + \rho_0\frac{\Gamma\Omega r}{2\pi}\Re\left\{\frac{i}{\zeta_v^*} + \frac{i}{\zeta_v - \zeta_s} - \frac{i}{\zeta_v^* - \frac{D_s^2}{4\zeta_s}}\right\}. \tag{21}$$

The loads acting on the polygonal-shaped strut are finally obtained from

$$F_{s,\phi}(t) = -\int_0^{2\pi} p(Z_s)x_t(\theta_s)\,d\theta_s, \quad F_{s,z}(t) = -\int_0^{2\pi} p(Z_s)y_t(\theta_s)\,d\theta_s. \tag{22}$$

These expressions for the forces per-unit-span can now be substituted into Eq. (17) to estimate the corresponding loading harmonics.

It is worth noting that, although the derivations presented in this section are tailored to a hypotrochoidal conformal mapping, the approach remains general and can be readily extended to other mapping functions Z. For example, aerofoil-shaped struts can be represented using a Kármán-Trefftz transform [35], while models for the potential flow past permeable bodies [37] can be employed to assess the interaction-noise mitigation achievable with porous struts, as recently demonstrated by Crawshaw et al. [38]. Similarly,

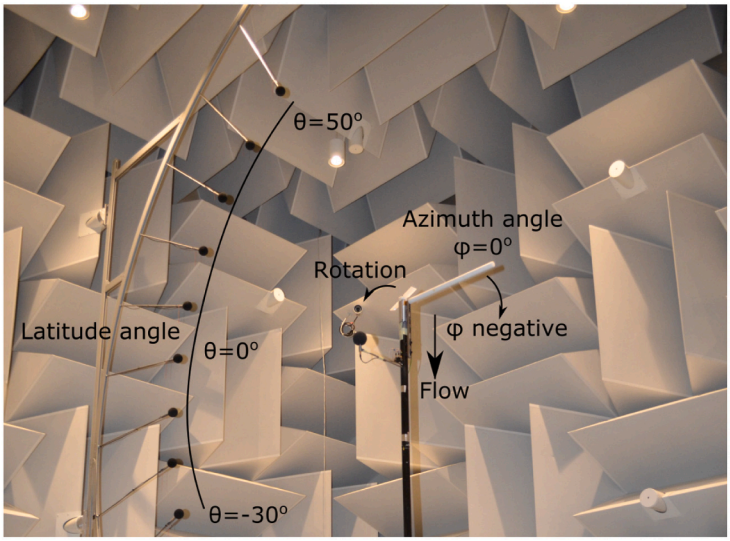

Fig. 5. Experimental setup from ISAE-SUPAERO for the propeller-strut interaction measurements carried out by Gojon et al. [13]. Picture taken from the open database published by Gojon and Jardin [14].

the method proposed by Baddoo and Ayton [39] for deriving the potential flow through an infinite cascade of aerofoils enables the analysis of multiple struts placed in close proximity, for which the superposition principle may no longer apply. Moreover, the methodology is applicable even when no closed-form conformal mapping is available, and the complex velocity must therefore be evaluated numerically, e.g. using lightning solvers, which provide a computationally-efficient means of computing potential flows in arbitrary domains [40].

3. Materials and methods

3.1. Experimental setup

The noise prediction methodology proposed in this paper is validated through comparison with the data included in the open database of Gojon and Jardin [14], which refers to the measurements from Gojon et al. [13] in the ISAE-SUPAERO anechoic chamber. Fig. 5 shows a picture of this experimental setup, which is briefly described below. The facility is characterised by a cut-off frequency of 80 Hz and is equipped to accommodate a rotor test stand, allowing the installation of a propeller-strut arrangement (see Fig. 5) with the possibility of varying the vertical distances of the strut from the rotor disc plane. Rotor actuation is provided by a Faulhaber 3274G024BP4-3692 brushless DC motor, while rotational speed, measured in revolutions per minute (rpm), is monitored and regulated in real time through an MC5010 motion controller. Aerodynamic loads are recorded using a six-axis ATI Nano17 load cell located directly below the motor.

Far-field acoustic measurements were performed by means of a directivity array equipped with 13 GRAS 40PH CCP free-field microphones. The array was placed at $R = 1.62\,\mathrm{m}$ from the rotor centre, corresponding to approximately eight rotor diameters, and spanned polar angles from $\theta_{\mathrm{exp}} = -\pi/3$ to $\theta_{\mathrm{exp}} = \pi/3$ in increments of $\Delta\theta_{\mathrm{exp}} = \pi/18$, with 0 defined at the rotor disc plane. The test rig was mounted on a turntable that allows azimuthal rotation of the rotor-strut assembly along the rotor disc plane in steps of $\Delta\phi_{\mathrm{exp}} = \pi/18$. The combined use of the directivity array and turntable enabled near-complete spherical directivity measurements, excluding the polar regions. Acoustic signals were sampled at a frequency of 51.2 kHz over a recording period of 16 s.

Several variations of rotors and struts were manufactured through stereolithography 3D printing. The rotor blades were based on a NACA 0012 aerofoil section, extruded along the span with a constant chord length of $c = 25\,\mathrm{mm}$ and a uniform pitch angle of $\alpha = \pi/18$, and were configured for clockwise rotation, meaning that Ω and Γ are negative. Each rotor had a tip radius of $r_{\mathrm{tip}} = 100\,\mathrm{mm}$ and a root radius of $r_{\mathrm{root}} = 16\,\mathrm{mm}$, with the number of blades ranging from $B = 2$ to $B = 4$. For these propellers, it is reasonable to expect that the assumption of acoustic compactness introduced in Section 2 remains valid up to $f \approx 3.4\,\mathrm{kHz}$, according to the compactness criterion proposed by Amiet [41]. The rotors were tested in conjunction with cylindrical struts of diameters $D_s = 10\,\mathrm{mm}$, 15 mm, and 20 mm, denoted as D10, D15, and D20, respectively, as well as struts with square and triangular cross-sections of side lengths $D_s = 10\,\mathrm{mm}$, indicated as S10 and T10, respectively. The rotational speeds were varied between 4000 rpm and 8000 rpm, although the acoustic results presented in this paper are only reported for the maximum speed, with the strut placed 20 mm below the rotor disc plane and the propeller orientated to direct its wake towards the strut. Here, the separation distance is defined as the gap between the rotor disc plane, taken as the plane intersecting the blades at the mid-chord, and the strut centreline, consistent with the parameter L defined in Section 2.

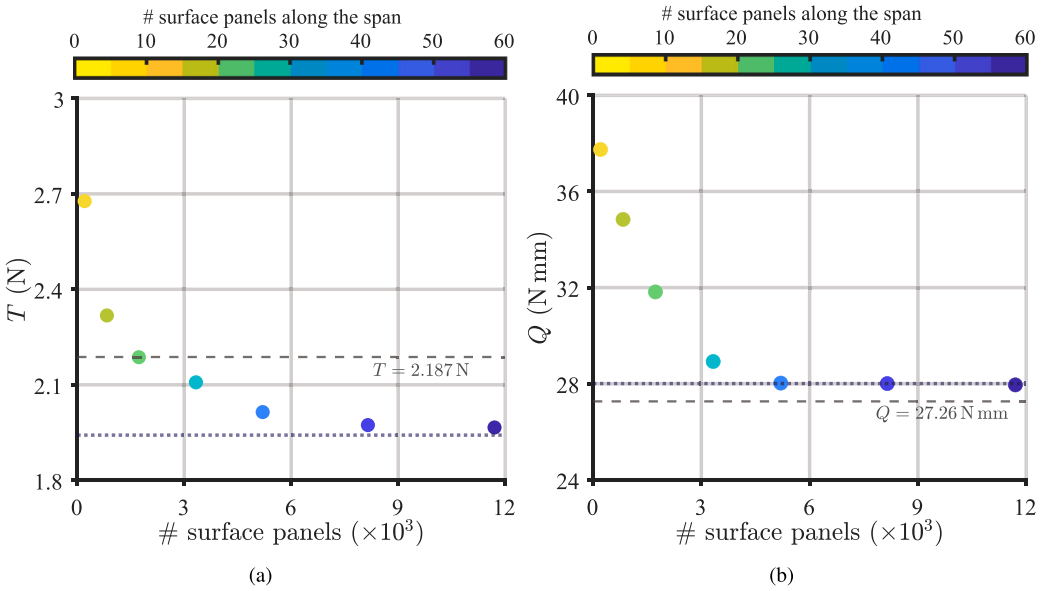

Fig. 6. Thrust and torque convergence studies for the two-bladed propeller at 8000 rpm for different levels of mesh refinements. The number of surface panels along the span is indicated in the colour bar, while the dotted lines denote the Richardson extrapolation.

3.2. Numerical simulation

The numerical simulations in this study are carried out using FlightStream®, a commercial unsteady panel software based on the surface vorticity method. The solver incorporates a Prandtl-Glauert correction to account for compressibility effects and a viscous correction that couples the potential flow field with a boundary-layer integral formulation [42]. In this framework, the propeller blades are modelled as impermeable surfaces carrying source and doublet distributions. In contrast, the wake is represented as a vortex sheet discretised into filaments, which are shed from the trailing edges by the Kutta condition and convected along with the local velocity.

The setup of the simulation environment and the mesh convergence analysis are performed for the two-bladed propeller operating at 8000 rpm. At 80 % of the blade span, where most aerodynamic loads are concentrated, the Mach and Reynolds numbers based on c are approximately 0.2 and 1.15×10^5, respectively. We employ a transitional boundary-layer model to capture the onset of flow transition, which affects both thrust production and skin-friction losses. A semi-empirical separation model based on the Valarezo-Chin criterion [43] is used to detect flow detachment at the blade tip by monitoring the pressure recovery along the suction side. Once separation is detected and its location identified, semi-empirical pressure values are applied to the separated surfaces. Finally, the vorticity-based formulation of the solver enables the inclusion of an induced-drag correction, computed from the integrated circulation and the downwash at the blade trailing edges.

The mesh convergence study is conducted by comparing the experimental data with the predicted steady thrust and torque values obtained for different mesh resolutions. We evaluated seven meshes with progressively increasing refinement. In all cases, the chordwise-to-spanwise resolution ratio is kept constant at 3.25, while a two-sided clustering is applied in both directions to refine the blade tip, root, and the leading and trailing edges. The total number of surface panels per blade is determined by the product of the chordwise and spanwise discretisations. The outcome of this analysis is illustrated in Fig. 6. Mesh convergence is considered achieved when more than 5200 surface panels per blade are used, corresponding to 130 chordwise and 40 spanwise stations. Here, the variations in thrust and torque relative to the finest mesh considered, i.e. for 11700 surface panels, are 2.46 % and 0.27 %, respectively, while the variations relative to the extrapolated Richardson solution [44] are 2.55 % and −0.04 %, respectively. Moreover, the converged solution yields a thrust deviation of −7.92 % and a torque deviation of 2.79 % compared to the experimental measurements. These trends differ from typical panel-method predictions, which generally produce accurate thrust estimates but tend to significantly overpredict torque, indicating that certain viscous transitional mechanisms may not be fully captured by the simplified models employed. In this regard, high-fidelity simulations conducted by Shenoy et al. [45] on a similar configuration showed that a laminar separation bubble with turbulent reattachment develops in the outboard region of the blade at high rotational speeds, extending over a large portion of the chord. The Valarezo-Chin criterion can detect the onset of this separation, but it does not resolve the boundary-layer dynamics or the subsequent reattachment. As a result, the laminar separation bubble is effectively modelled as a local loss of lift rather than a transitional region with pressure recovery.

Fig. 7 provides a visualisation of the instantaneous flow field of the two-bladed propeller after four revolutions, illustrating the wake filaments shed at the blade trailing edges and the roll-up of the tip vortices. The first three revolutions correspond to a transient during which the propeller-induced velocity builds up and the wake is convected downstream at progressively higher speeds. By the

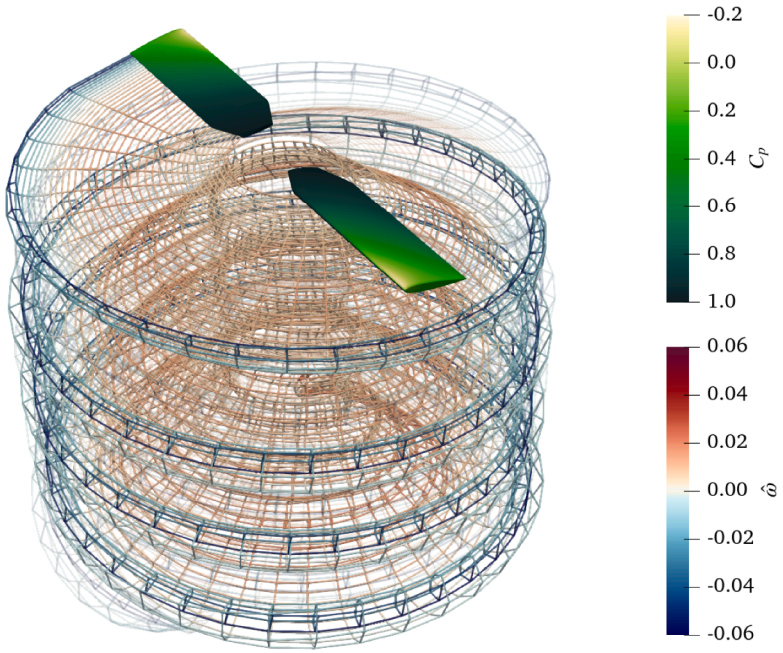

Fig. 7. Visualisation of the instantaneous flow field after four revolutions of the propeller. The colour scale on the blade indicates the surface pressure coefficient C_p, while that on the wake filaments denotes the normalised vorticity $\hat{\omega}$. The wake shed by one blade is rendered transparent for improved clarity.

fourth revolution, the induced velocity reaches a steady value, although the start-up wake still forms a stagnating vorticity region that causes oscillations in blade loading. To mitigate this effect, the solver implements a wake-termination feature that retains only the wake filaments shed during the last user-specified iterations and discards the older ones. Since statistical convergence of the aerodynamic loads can be achieved by considering the wake shed over a single propeller revolution [46], the wake-termination tool is configured here to retain only the filaments associated with the fourth revolution.

In each simulation, the time increment is chosen to produce an angular advancement of approximately $\pi/18$ per iteration. With this temporal resolution and setup, and for 5200 surface panels, the computation of one propeller revolution requires less than 5 min on 8 CPU cores of a commodity laptop with AMD Ryzen 7 PRO 7840U processors. For comparison, the large-eddy simulation of the same propeller from Shenoy et al. [45], run on 4664 CPU cores, required about 1.37 h per revolution.

Simulations were carried out for blade numbers of $B = 2,\ 3$ and 4 and a range of rotational velocities from 4000 rpm to 8000 rpm with increments of 1000 rpm. The results are reported in Fig. 8. For the two-bladed propeller, the numerical computations systematically underpredict thrust across all operating points. A nearly constant offset is found between the computed and measured thrust, which implies that the relative error decreases with increasing rotational speed. The torque is well captured across the speed range, showing a slight overestimation at lower speeds and a slight underestimation at higher speeds.

Overall, for even-bladed rotors, the performance predictions agree well with the measurements. The three-bladed configuration, however, shows increasing discrepancies between predicted and experimental loads as the rotational speed increases. Gojon et al. [9] observed that the ISAE-SUPAERO three-bladed rotor is more efficient than the four-bladed configuration, delivering the same thrust with lower torque at high rotational speeds. This behaviour has been attributed to competing mechanisms associated with low Reynolds-number effects, blade-vortex interactions, and reduced blade loading [47], phenomena that the solver does not model with sufficient fidelity. An evaluation of how these limitations affect the noise predictions will be presented in Section 4.1.

3.3. Model inputs and test matrix

The analytical models presented in Section 2 are adapted to reproduce the experimental setup of Gojon et al. [13]. The ambient conditions are set at $\rho_0 = 1.20\,\mathrm{kg\,m^{-3}}$ and $c_0 = 340\,\mathrm{m\,s^{-1}}$, and the blade geometry is discretised using the chord and pitch parameters of the ISAE-SUPAERO propeller outlined in Section 3.1. The spherical reference frame used in the experimental arrangement is related to that of the analytical formulation through the transformation $(R, \Theta, \Phi) = (R, \pi/2 - \theta_{\mathrm{exp}}, \pi - \phi_{\mathrm{exp}})$, proposed by Vella et al. [22]. Within this coordinate system, the strut is positioned at $\Phi = 0$, equivalent to $\phi_{\mathrm{exp}} = \pi$, as depicted in Fig. 1.

Our prediction method requires as input the steady loading distribution of the isolated propeller along the radius estimated in Section 3.2, i.e. in the absence of the strut. In fact, we assume that the strut has a negligible influence on the mean aerodynamic performance of the propeller under hovering conditions, while its unsteady aerodynamic effects are accounted for analytically based on this distribution. The axial and tangential components of the propeller induced velocity $\boldsymbol{U_i}$ are then calculated from these steady

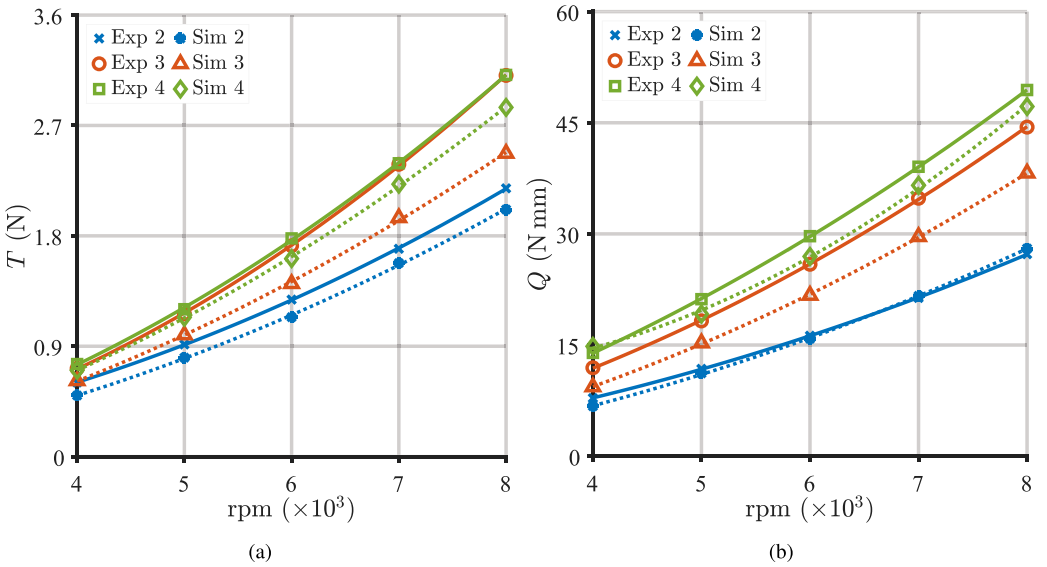

Fig. 8. Comparison of experimental and simulated (a) thrust and (b) torque for propellers with different blade numbers $B = 2,\ 3$ and 4 (indicated by the number in the legend). Solid and dashed lines represent quadratic polynomial fits to the experimental and simulation data, respectively.

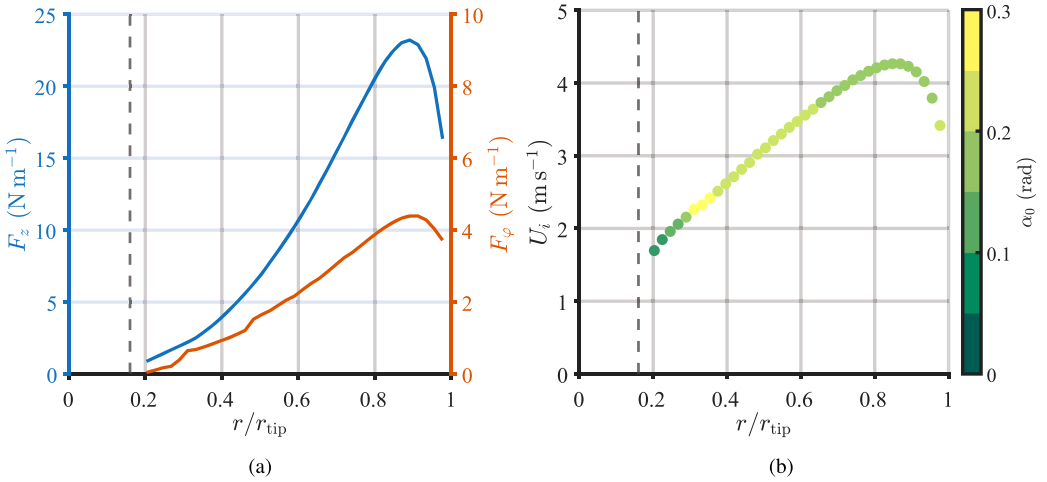

Fig. 9. (a) Axial and tangential loading distributions along the propeller blade span. (b) Induced velocity magnitude distribution generated by the propeller, where symbol colours represent the corresponding flow swirl angles. The data refer to the case with $B = 2$, and the vertical dashed lines indicate the propeller root.

loads. In this case, we model the rotor as an idealised actuator disc imparting a pressure jump to the flow. Considering the annular ring of radius r and width $\mathrm{d}r$ on the disc in Fig. 1, the sectional thrust $\mathrm{d}T$ is related to the axial induced velocity $U_{i,z}$ by momentum theory, according to

$$U_{i,z} = \sqrt{\frac{\mathrm{d}T}{4\pi\rho_0 r \mathrm{d}r}}. \tag{23}$$

The tangential induced velocity $U_{i,\phi}$ arises from the swirling motion imparted by the propeller. Imposing conservation of angular momentum makes it possible to relate this velocity component to the sectional torque $\mathrm{d}Q$ applied by the propeller, yielding

$$U_{i,\phi} = \frac{\mathrm{d}Q}{4\pi\rho_0 r^2 \mathrm{d}r U_{i,z}}. \tag{24}$$

The flow swirl angle is finally obtained from $\alpha_0 = \arctan\left(U_{i,\phi}/U_{i,z}\right)$. Fig. 9 shows an example of the loading distributions and the resulting induced velocities and flow swirl angles for the two-bladed propeller used as input in the analytical model.

It is relevant to stress that, as mentioned in Section 2.1, this discretisation of the induced velocity field does not incorporate the effects of flow acceleration due to slipstream contraction, which is a necessary simplification to maintain the uniform-stream

Table 1
Test matrix considered for the validation of the analytical modelling among those included in the database of Gojon and Jardin [14]. The data refer to a constant rotational speed of 8000 rpm.

	D10	D15	D20	T10	S10
$B = 2$	✓	✓	✓		✓
$B = 3$		✓			
$B = 4$		✓			

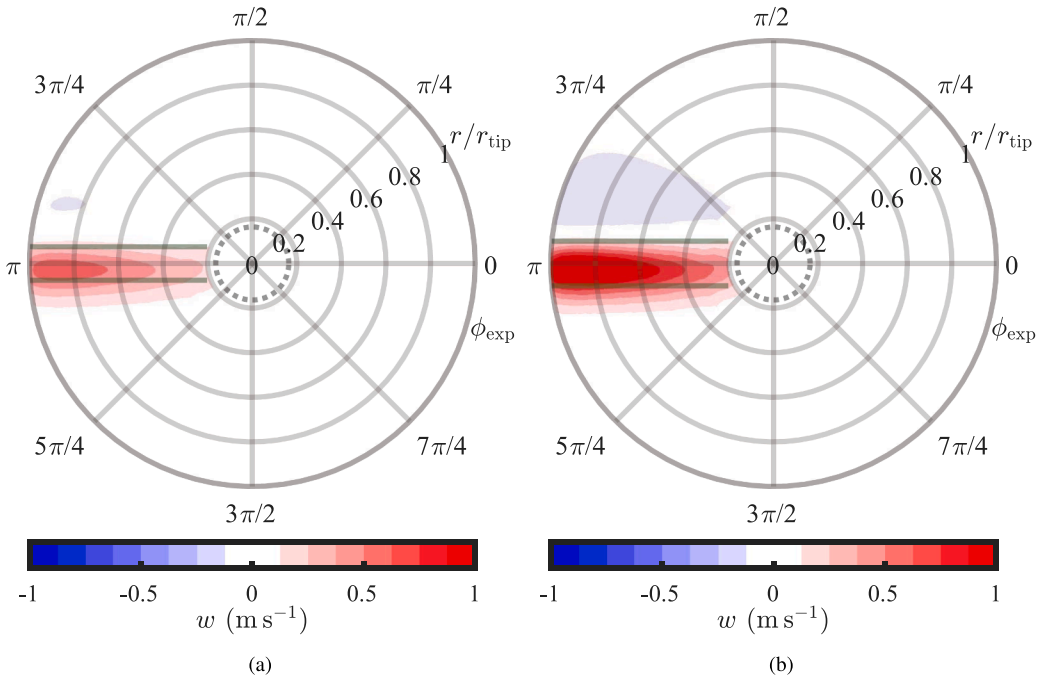

Fig. 10. Contours of the upwash velocity disturbance induced by the (a) D15 and (b) D20 struts at $L = 20$ mm. The propeller spins clockwise.

assumption when computing the flow potential f. Moreover, we ignore three-dimensional effects occurring at the blade tip. The impact of these simplifications on noise prediction will be assessed in Section 4.

Finally, the proposed prediction methodology is validated against various propeller-strut configurations contained in the open database of Gojon and Jardin [14], including different rotor blade numbers, strut diameters, and strut shapes. An overview of the resulting test matrix is provided in Table 1.

4. Results and discussion

In this section, we compare the results of the analytical calculations with the experimental data. We first apply the model to struts with circular cross-sections, illustrating the influence of strut diameter and propeller blade number on the radiated noise. The analysis is then extended to non-circular cross-sections, making use of the hypotrochoidal conformal mapping introduced in Section 2.4. Finally, we employ the analytical framework to predict the noise generated by a propeller in the presence of struts with spanwise-varying cross-sections, demonstrating its potential as an optimisation tool for UAV designs.

4.1. Struts with circular cross-sections

The upwash disturbance defined in Eq. (3) directly affects the unsteady lift generated by the blade segment through Sears' theory. Therefore, the analysis of this velocity component is indicative of the sources of unsteady loading noise radiated by the blade. For this purpose, the w contours on the propeller disc are shown in Fig. 10a and b for the D15 and D20 struts, respectively. As expected, the strut with the larger diameter induces a broader and more intense flow distortion region on the propeller disc, concentrated around $\phi_{\text{exp}} = \pi$. Due to the flow swirl angle, each blade experiences the blockage imposed by the strut before passing over the component, whereas a region of induced-velocity increase, associated with negative upwash, develops past it. For both strut configurations, higher w values are concentrated near the blade tip region ($r/r_{\text{tip}} \approx 0.8 - 0.9$), in agreement with the U_i distribution shown in Fig. 9b. Consequently, the dominant sources of blade unsteady loading noise are expected to originate from this region.

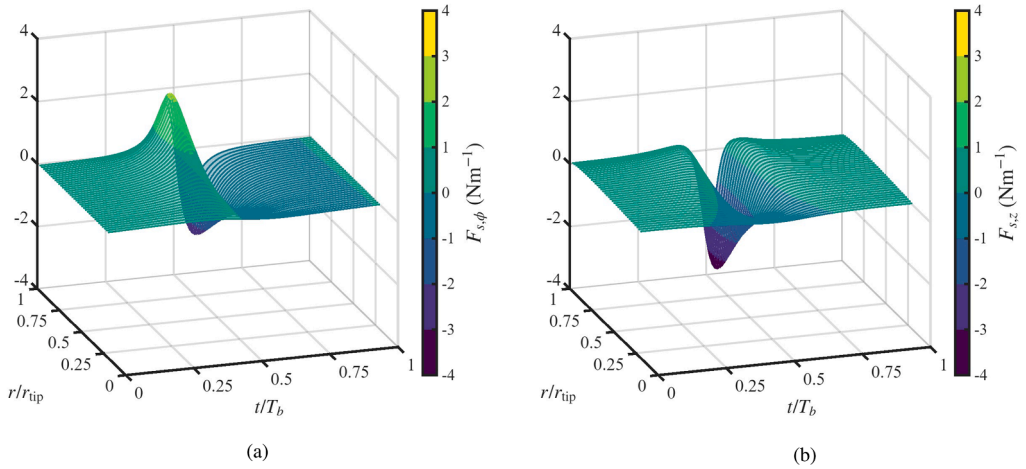

Fig. 11. Time-varying (a) tangential and (b) axial forces per unit span exerted on the D15 strut at $L = 20\,\text{mm}$ due to the passage of the blade at different radial stations during one period T_b. The data refer to the case for $B = 2$.

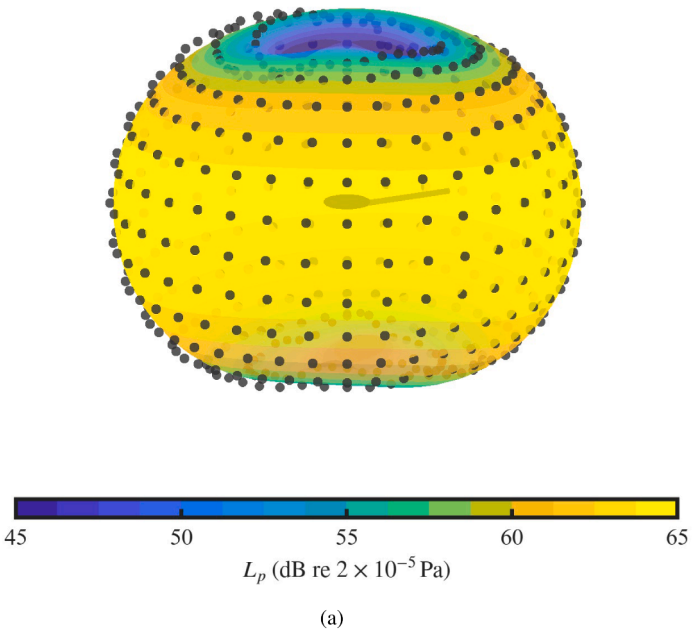

Fig. 12. Predicted directivity pattern of the far-field noise radiated at the BPF by the two-bladed propeller with the D15 strut at $L = 20\,\text{mm}$. The black dots denote the corresponding experimental measurements.

A similar scenario characterises the unsteady loads on the strut produced by the blade passage. The time-varying $F_{s,\phi}$ and $F_{s,z}$ distributions for the D15 strut and the two-bladed propeller over one period T_b are shown in Fig. 11a and b, respectively. Both loads exhibit impulsive behaviour confined to the short time interval in which the blade is in close proximity to the strut. This result supports expanding $F_{s,\phi}$ and $F_{s,z}$ in Fourier series to represent the periodic nature of the strut unsteady loading, as the effects of two consecutive blade passages are sufficiently separated, and their individual contributions can be linearly superposed. This assumption was also confirmed for configurations with more blades, which correspond to shorter periods T_b, though those results are omitted here for brevity. Moreover, while the tangential loading distribution features a sign inversion that depends on whether the blade is approaching or moving away from the strut, the axial one remains mostly negative and reaches a larger magnitude, suggesting a dominant contribution to the radiated noise. Likewise, the peak of these unsteady loading distributions occurs at $r/r_{\text{tip}} \approx 0.8 - 0.9$ due to the higher values of Γ at this radial location, which are predominantly determined by steady loads and, in turn, influence the strength of the point vortices representing the blade passage.

The accuracy in modelling the aerodynamic quantities discussed above determines the prediction of potential-interaction noise. The total far-field acoustic pressure is obtained by incoherently summing the contributions of the rotor, comprising blade loading

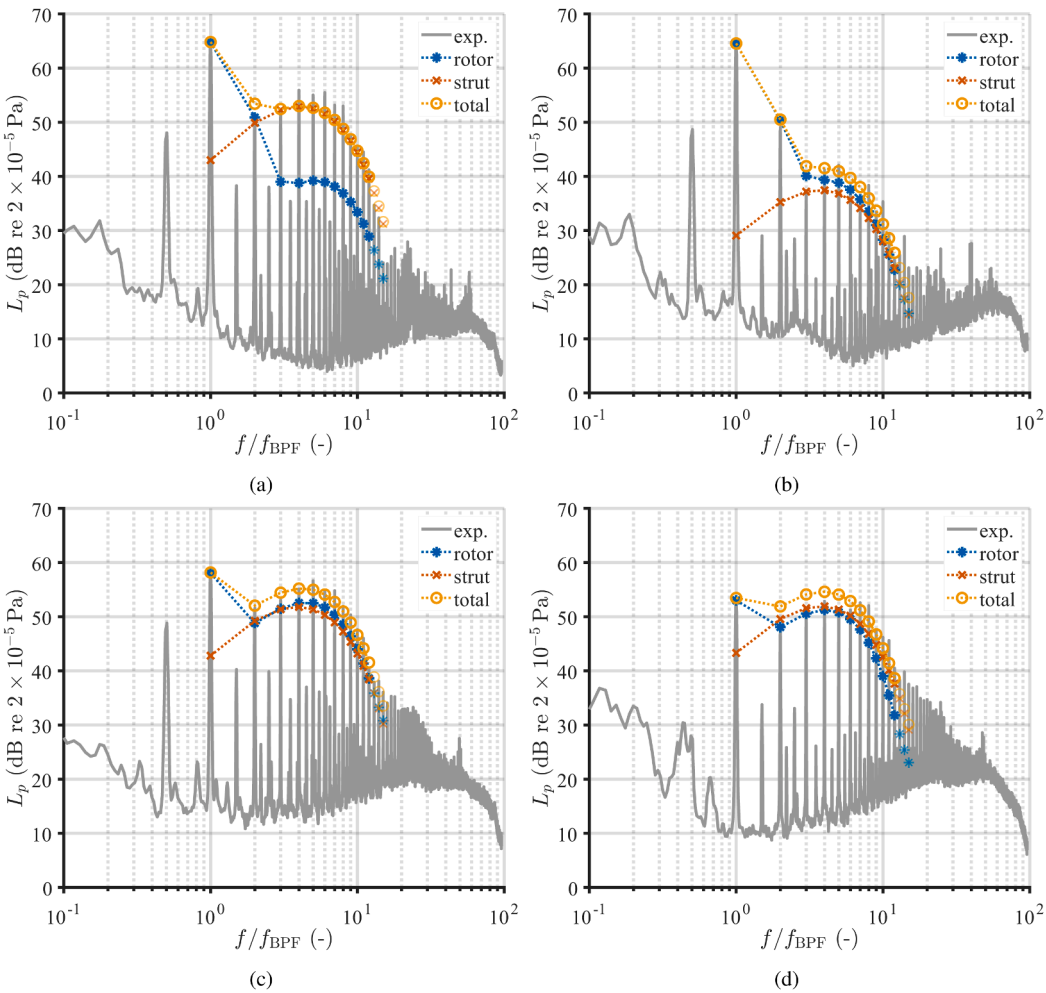

Fig. 13. Experimental spectra and predicted harmonics of the far-field noise radiated by the two-bladed propeller with the D15 strut at $L = 20$ mm for (a) $[\theta_{\mathrm{exp}}, \phi_{\mathrm{exp}}] = [0, \pi/2]$, (b) $[\theta_{\mathrm{exp}}, \phi_{\mathrm{exp}}] = [\pi/18, 0]$, (c) $[\theta_{\mathrm{exp}}, \phi_{\mathrm{exp}}] = [5\pi/18, 5\pi/18]$, and (d) $[\theta_{\mathrm{exp}}, \phi_{\mathrm{exp}}] = [-\pi/3, 8\pi/9]$. The frequency axis is normalised by the BPF, whereas the transparent markers denote conditions for which the acoustic compactness assumption imposed in the analytical model is no longer valid.

(Eq. (1)) and thickness noise (Eq. (9)), and of the strut (Eq. (10)), reflecting the weakly coupled nature of the implemented models. In the subsequent analysis, we compute the sound pressure levels L_p with a reference pressure of 2×10^{-5} Pa. Fig. 12 shows the resulting radiation pattern generated by the two-bladed propeller operating upstream of the D15 strut at the BPF, together with the experimental data. At this frequency, the propeller-strut configuration exhibits the typical toroidal directivity of rotor steady loading noise, with maximum sound levels radiated sideways in the rotor plane and minima along its axis. No effect of the strut is observed, as noise at the fundamental frequency for a two-bladed propeller is expected to be determined solely by the mean aerodynamic performance of the rotor and by the blade thickness. An excellent qualitative agreement is found between the prediction and the measurements throughout the domain.

The computed BPF harmonics of the far-field pressure for the same propeller-strut configuration are compared with the experimental spectra in Fig. 13 for several observer positions. Rotor and strut noise levels are shown separately, as well as their overall contribution. In addition, only the BPF harmonics for which the assumption of acoustic compactness holds are highlighted (see Section 3.1). For all considered locations, the model predicts the BPF amplitude within 1 dB, supporting the qualitative observations from Fig. 12 and confirming that the contribution of strut loading noise at the fundamental frequency is negligible. When the observer lies within the propeller disc and normal to the strut axis (Fig. 13a), noise at higher BPF harmonics predominantly originates from the strut, as previously reported by Gojon et al. [13]. The analytical model accurately reproduces the envelope of the frequency hump centred on the fifth harmonic, with deviations generally below 1 dB, except between the fourth and seventh harmonics, where the noise is slightly underestimated. These discrepancies may be attributed to physical mechanisms not captured by the model, such as flow-separation effects or tip-vortex interactions. Interestingly, although its contribution to the harmonics is negligible, the unsteady loading noise from the blades remains of the same order as the envelope of the sub-harmonics occurring at multiples of the shaft frequency 0.5 BPF, which are attributable to possible rotor imbalance [13].

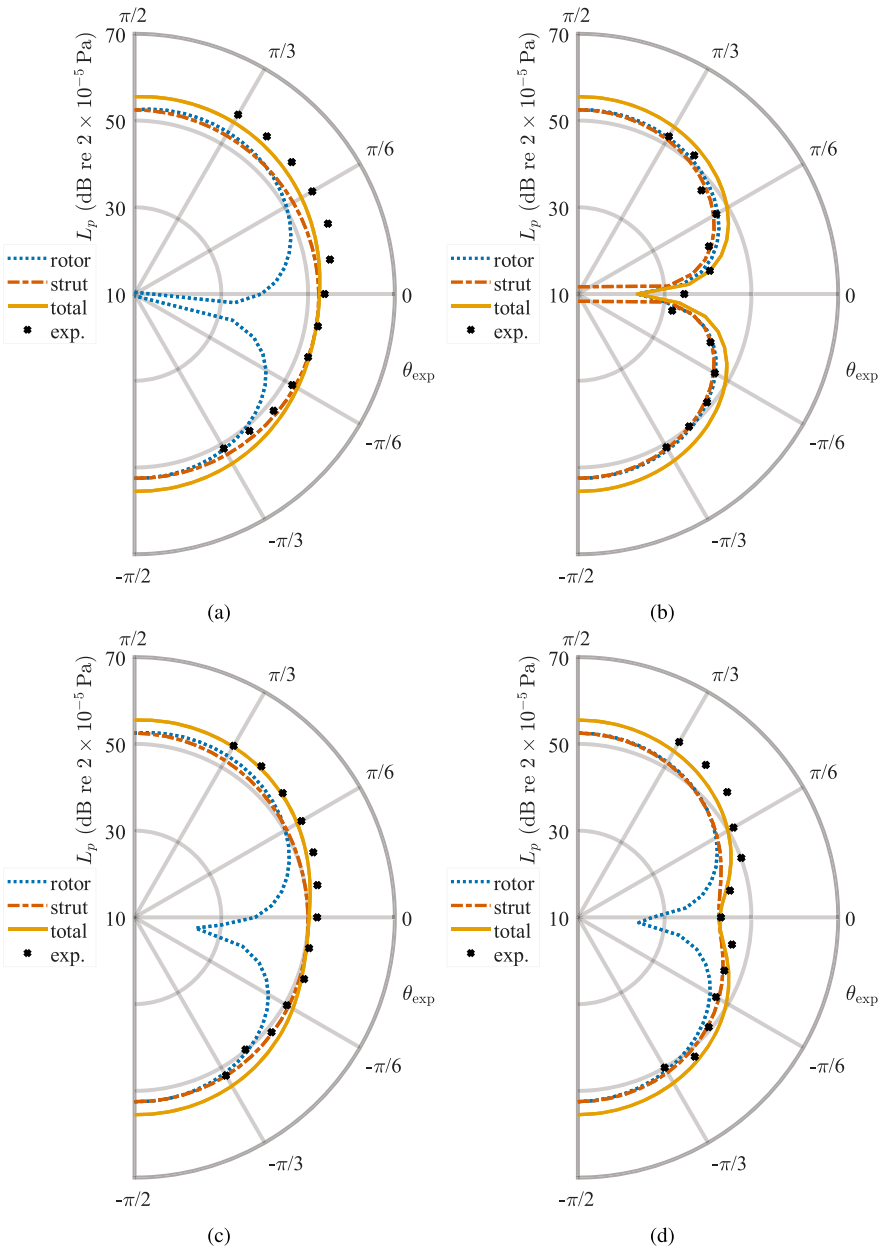

Fig. 14. Experimental and predicted directivity patterns of the far-field noise radiated at the fifth harmonic of the BPF by the two-bladed propeller with the D15 strut at $L = 20\,\text{mm}$ for (a) $\phi_{exp} = \pi/2$, (b) $\phi_{exp} = 0$, (c) $\phi_{exp} = 5\pi/18$, and (d) $\phi_{exp} = 8\pi/9$.

We also observe a general satisfactory agreement between the analytical calculations and the measurements when the observer lies in the immediate vicinity of the strut axis (Fig. 13b). In this case, the noise radiated by the rotor exceeds that produced by the strut up to the tenth BPF harmonic, because the observer is located near the direction of minimum radiation of the dipole associated with strut loading noise, i.e. along its axis[1] At the third BPF harmonic, the predicted sound pressure level overestimates the experimental level, which might be related to destructive interference between noise sources that is not encompassed by the model, as the rotor and strut contributions are summed incoherently.

When the observer is positioned at an intermediate azimuthal angle and at a positive polar angle away from the rotor disc (Fig. 13c), the predicted overall noise agrees well with the experimental spectra, and the harmonic envelope is accurately captured.

[1] Since the strut does not radiate along its axis, the strut loading noise model is not defined at $[\theta_{exp}, \phi_{exp}] = [0, 0]$; this observer location is therefore excluded from the present analysis.

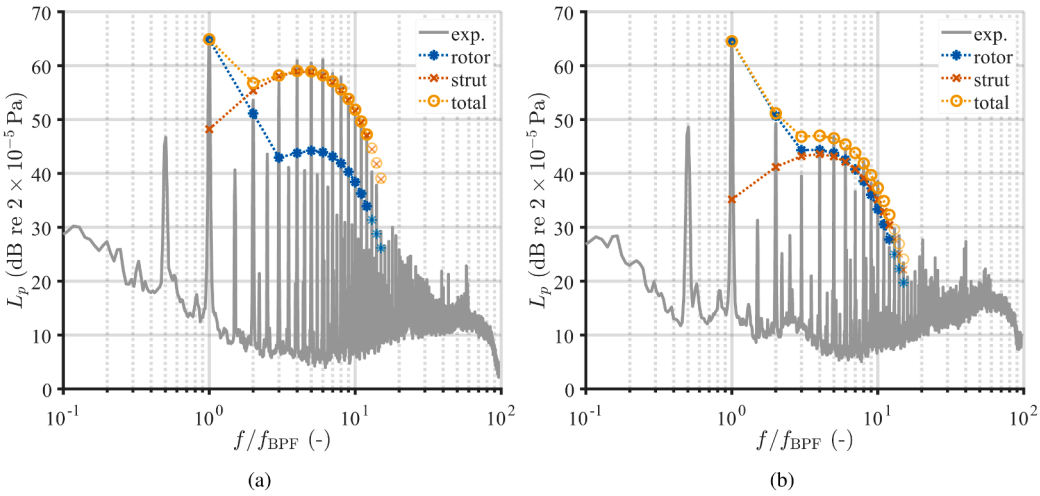

Fig. 15. Experimental spectra and predicted harmonics of the far-field noise radiated by the two-bladed propeller with the D20 strut at $L = 20\,\mathrm{mm}$ for (a) $[\theta_{\mathrm{exp}}, \phi_{\mathrm{exp}}] = [0, \pi/2]$ and (b) $[\theta_{\mathrm{exp}}, \phi_{\mathrm{exp}}] = [\pi/18, 0]$. The frequency axis is normalised by the BPF, whereas the transparent markers denote conditions for which the acoustic compactness assumption imposed in the analytical model is no longer valid.

In contrast, when it is placed at negative polar angles (Fig. 13d), the analytical calculations consistently overestimate the experimental data for frequencies ranging from the second to the sixth BPF harmonics. A partial shielding effect in the measurements, caused by the presence of the strut between the propeller and the microphones, could potentially contribute to this trend for $\pi/2 < \phi_{\mathrm{exp}} < 3\pi/2$.

The radiation patterns of the far-field pressure computed at the azimuthal observer positions from Fig. 13 are shown in Fig. 14 for the fifth BPF harmonic, which is representative of the frequency hump associated with the potential-interaction contribution. In general, the analytical model accurately predicts both the shape and amplitude of the experimental directivity profiles. In most cases, the unsteady loading noise from the strut is found to dominate over that from the rotor, except at angles close to its axis, confirming the findings of Gojon et al. [13]. Furthermore, the asymmetry in the radiation pattern observed in the measurements is not captured by the prediction method, resulting in a slight underestimation at positive polar angles and a slight overestimation at negative ones, as observed in the spectra in Fig. 13c, and d. Similarly, this behaviour could be attributed to phase-interference effects not considered in the estimation of strut loading noise.

The results discussed above confirm that the proposed prediction method successfully describes the noise radiated by the rotor and strut due to potential interactions for a specific propeller-strut arrangement. The focus is now shifted to assessing whether the model can reproduce the effects of changes in the geometrical parameters of the system. For the sake of brevity, only the sound pressure levels at two observer locations are considered in the following. Fig. 15 shows the comparison between the predicted BPF harmonics and the experimental spectra for the two-bladed propeller operating upstream of the D20 strut while maintaining the same rotor-strut separation distance as before. This configuration was selected by Vella et al. [22] for the validation of their prediction methodology. In general, the same considerations made for Fig. 13 also apply to the larger strut. The total L_p value at the BPF remains unchanged, as the different strut has only a negligible influence on the steady loads of the propeller. Also in this case, for an observer on the propeller disc and normal to the strut axis (Fig. 15a), the model for the strut unsteady loading noise captures the envelope of the frequency hump centred on the fifth harmonic, although still with a slight underestimation of its levels, while the model for the blade unsteady loading noise is closer to the frequency hump associated with the sub-harmonics. Moreover, the same overestimation occurring at the third BPF harmonic for an observer orientated near the strut axis (Fig. 15b) is maintained here.

The satisfactory agreement between the analytical predictions and the experimental data for the D20 case also extends to the directivity patterns at the fifth harmonic for $\phi_{\mathrm{exp}} = \pi/2$ and $\phi_{\mathrm{exp}} = 0$, which are shown in Fig. 16a and b, respectively. Although the prediction method is unable to reproduce the asymmetric distribution observed in the measurements, the deviation for positive polar angles is smaller than in the D15 case and does not exceed 3 dB. This result indicates that the model correctly captures the dominant physical mechanisms governing the propeller-strut potential interaction and that the simplifications made in the mathematical derivations, e.g. in the discretisation of the induced velocity of the propeller (see Section 3.3), do not significantly compromise the noise prediction accuracy.

We obtain a similar outcome for a strut with a smaller circular cross-section. The predicted BPF harmonics of the far-field pressure for the two-bladed propeller operating upstream of the D10 strut are compared with the measurements in Fig. 17, whereas the corresponding radiation patterns are shown in Fig. 18. As in the other configurations, for an observer lying within the propeller disc and normal to the strut axis (Fig. 17), the model accurately predicts the sound pressure level at the BPF and the envelope of the frequency hump around the fifth harmonic, although the experimental data are slightly more underestimated, particularly at the second BPF harmonic. The more pronounced underprediction is also evident in the directivity profile at $\phi_{\mathrm{exp}} = \pi/2$ (Fig. 18a), especially for positive polar angles. These results are consistent with the previously observed trend, in which higher D_s values lead to more accurate strut loading noise predictions. The situation differs for an observer located near the strut axis (Fig. 17b), where the

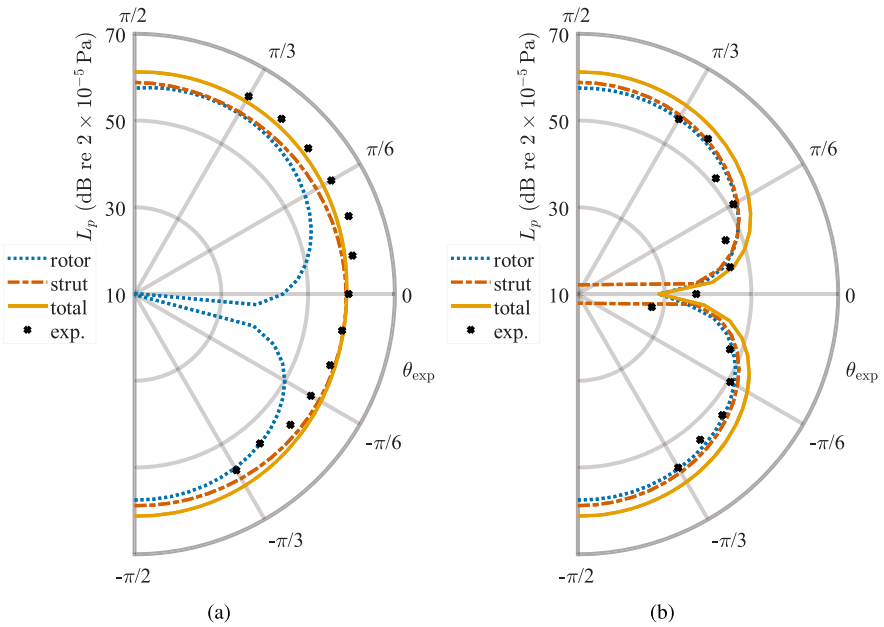

Fig. 16. Experimental and predicted directivity patterns of the far-field noise radiated at the fifth harmonic of the BPF by the two-bladed propeller with the D20 strut at $L = 20\,\text{mm}$ for (a) $\phi_{exp} = \pi/2$ and (b) $\phi_{exp} = 0$.

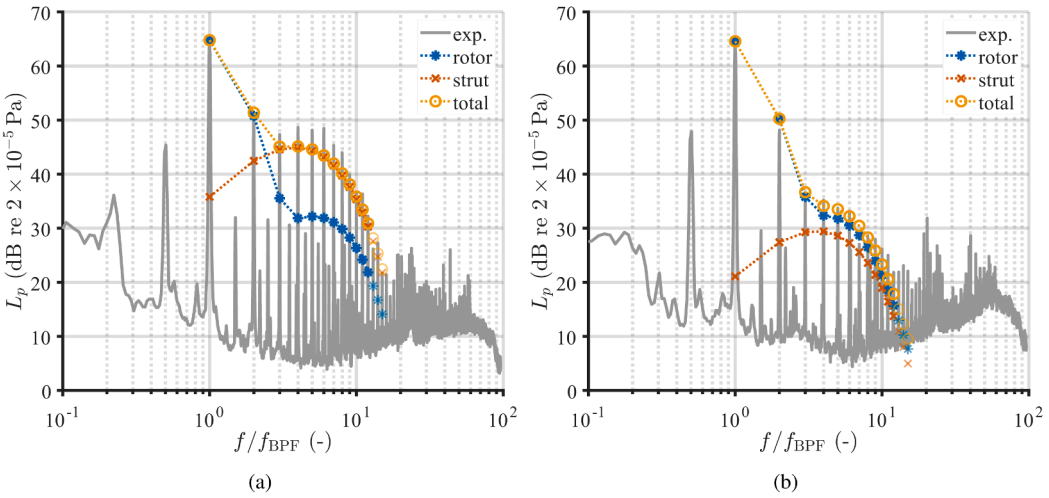

Fig. 17. Experimental spectra and predicted harmonics of the far-field noise radiated by the two-bladed propeller with the D10 strut at $L = 20\,\text{mm}$ for (a) $[\theta_{exp}, \phi_{exp}] = [0, \pi/2]$ and (b) $[\theta_{exp}, \phi_{exp}] = [\pi/18, 0]$. The frequency axis is normalised by the BPF, whereas the transparent markers denote conditions for which the acoustic compactness assumption imposed in the analytical model is no longer valid.

rotor contribution dominates. In this case, the experimental levels are correctly reproduced, including that at the third BPF harmonic. Similarly, the comparison between the measurements and the analytical calculations at $\phi_{exp} = 0$ (Fig. 18b) exhibits a more consistent agreement due to the predominance of noise generated by the propeller.

Finally, increasing the number of blades is expected to influence the unsteady loads on the strut, as the time interval between consecutive blade passages decreases and the potential interactions that they induce occur more frequently. The predicted BPF harmonics and the corresponding experimental spectra for the three-bladed and four-bladed propellers operating upstream of the D15 strut are shown in Fig. 19 for the two considered observer positions. In these cases, the model slightly underpredicts the BPF peak, most likely due to a more pronounced underestimation of the steady loads by the numerical flow solver compared to the two-bladed configuration (see Fig. 8). Furthermore, the assumption that the presence of the strut does not affect the mean aerodynamic performance of the rotor becomes progressively less valid as the propeller solidity increases, as noted by Gojon et al. [13] (see Section 1). Focusing on higher frequencies, for $B = 3$ (Fig. 19a and b), the frequency hump centred on the fifth BPF harmonic is correctly predicted, with performance similar to the corresponding two-bladed propeller case.

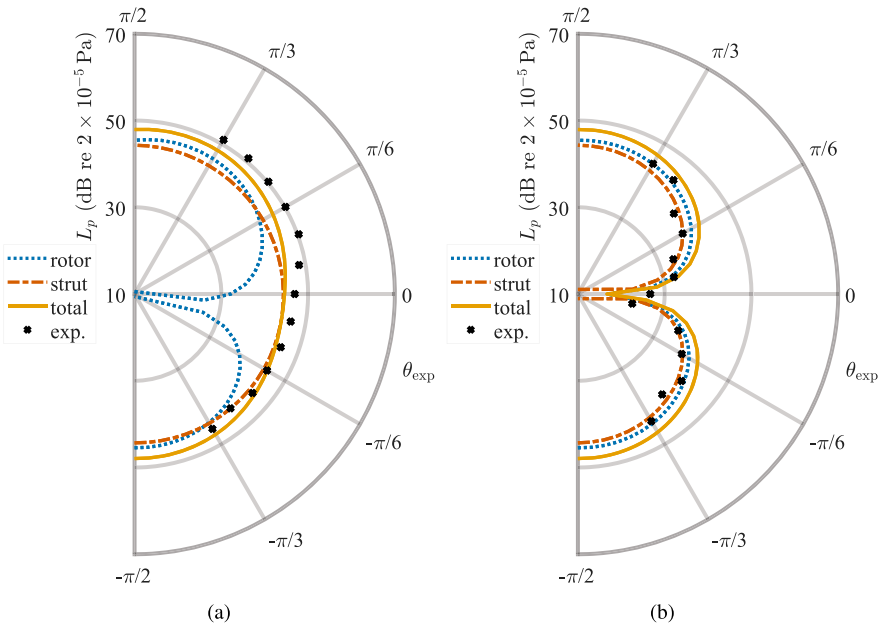

Fig. 18. Experimental and predicted directivity patterns of the far-field noise radiated at the fifth harmonic of the BPF by the two-bladed propeller with the D10 strut at $L = 20$ mm for (a) $\phi_{exp} = \pi/2$ and (b) $\phi_{exp} = 0$.

In contrast, for $B = 4$ (Fig. 19c , d), we observe two different trends. When the rotor noise dominates, i.e. for observers close to the strut axis, the experimental data are correctly reproduced, except for the discrepancy at the third BPF harmonic also observed in the previous results. Conversely, when the strut noise dominates, the envelope shape is captured, but the measured sound levels are significantly underpredicted, suggesting that, while the unsteady loading sources on the blades are well represented by the inflow-distortion modelling, those on the strut are not adequately estimated. This effect may result from a higher sensitivity of the flow-potential model in Eq. (12) to the aerodynamic input since the strength of the vortices that represent the blade passages is related to the steady thrust generated by the propeller.

4.2. Struts with non-circular cross-sections

A modification in the cross-section shape of the strut alters both the inflow distortion it induces on the propeller disc and the resulting unsteady loading imparted on its surface. Here, we consider the square cross-section strut tested by Gojon et al. [13], i.e. the S10 configuration, to assess the capability of the model to reproduce the potential interaction generated by struts with non-circular cross-sections. A representation of the potential flow past the S10 strut cross-section was previously shown in Fig. 4b, while Appendix A reports a list of different geometries that can be described using the proposed conformal mapping, including the T10 configuration from ISAE-SUPAERO.

Fig. 20 shows the comparison of the upwash disturbance contours on the propeller disc produced by the D10 and S10 struts. Despite having the same frontal area, the two strut configurations induce different inflow distortions due to the higher blockage, which, in turn, influences the unsteady loading noise from the propeller. The spanwise distribution of w is similar in both cases and reflects the corresponding induced velocity profile of the rotor. This implies that optimising the local cross-section of the strut by shape modification alone, while preserving structural integrity, is feasible and could reduce the inflow distortion in the region near the blade tip, which contributes most significantly to the radiated noise.

The predicted BPF harmonics for the two-bladed propeller operating upstream of the S10 strut are shown in Fig. 21, together with the experimental spectra for the same observer locations addressed above. Overall, the analytical calculations agree well with the measurements, successfully capturing the shape of the frequency-hump envelope and the corresponding sound levels, which feature slightly higher values with respect to the D10 case. This noise increase, previously reported by Gojon et al. [13], is directly linked to the stronger inflow distortion observed in Fig. 20. Interestingly, the measured frequency hump associated with the BPF sub-harmonics is considerably attenuated when compared to the circular cross-section strut. The origin of such a trend remains unclear at this stage.

The radiation patterns shown in Fig. 22 confirm the suitability of the method to predict the noise from this configuration. Fair agreement is achieved between the experimental and analytical results for $\phi_{exp} = \pi/2$ (Fig. 22a), while the model slightly overpredicts the measurements for $\phi_{exp} = 0$ (Fig. 22b). By comparing these results with the directivity profiles in Fig. 18, it appears that the noise increase on the rotor disc due to the more significant potential distortion is not maintained throughout the range of polar angles, especially for $\pi/6 \leq \theta_{exp} \leq \pi/3$, where comparable sound levels are observed. This behaviour suggests that the underestimation

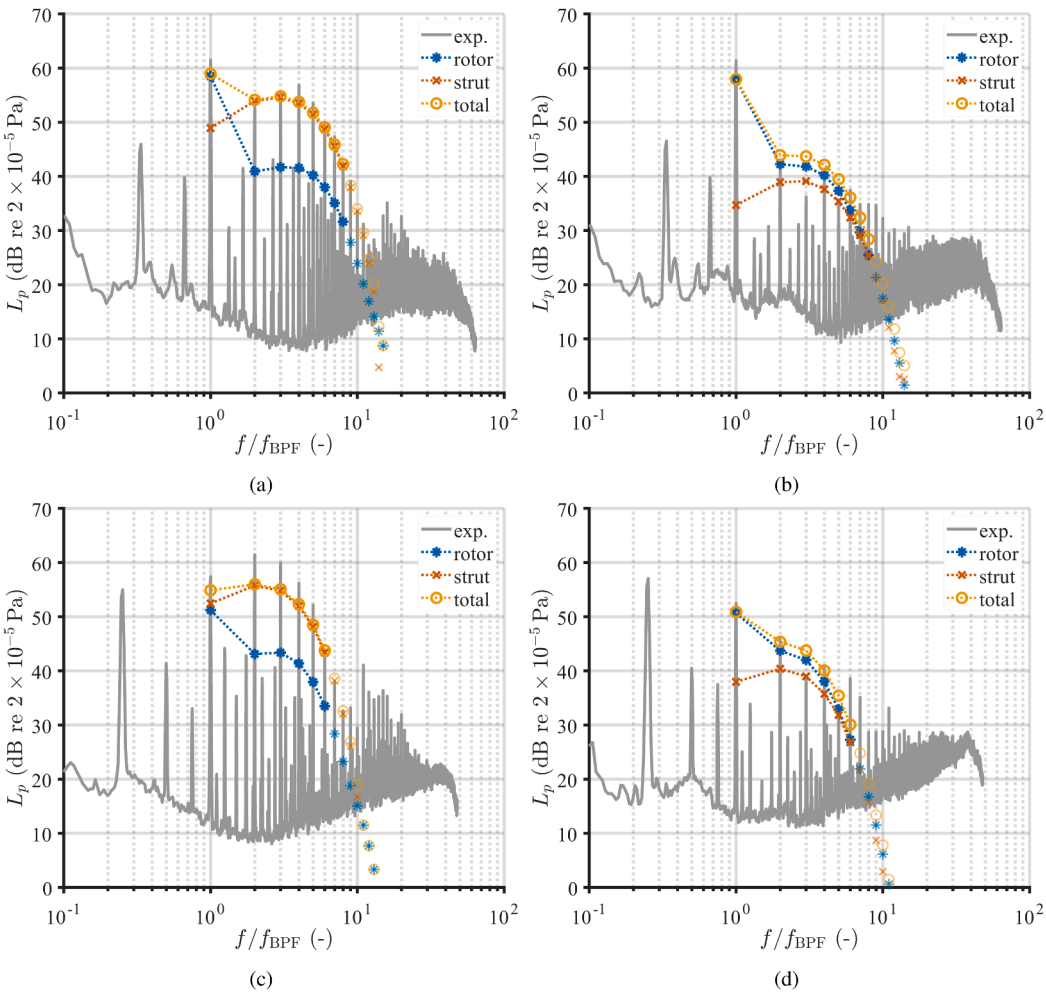

Fig. 19. Experimental spectra and predicted harmonics of the far-field noise radiated by the (a,b) three-bladed and (c,d) four-bladed propellers with the D15 strut at $L = 20\,\mathrm{mm}$ for (a,c) $[\theta_{\mathrm{exp}}, \phi_{\mathrm{exp}}] = [0, \pi/2]$, and (b,d) $[\theta_{\mathrm{exp}}, \phi_{\mathrm{exp}}] = [\pi/18, 0]$. The frequency axis is normalised by the BPF, whereas the transparent markers denote conditions for which the acoustic compactness assumption imposed in the analytical model is no longer valid.

observed at positive polar angles for both the D10 and S10 strut configurations may result from an additional noise contribution not accounted for by the analytical model and that is less sensitive to the strut architecture.

4.3. Struts with spanwise-varying cross-sections

In the previous sections, we extensively validated the proposed analytical framework for different propeller-strut arrangements and far-field observers. The objective is now to employ it to infer general trends and guidelines for the aeroacoustic optimisation of integrated propeller-airframe designs by investigating the geometrical parameters that can minimise potential-interaction noise. To this end, the effect of the propeller-strut distance on the unsteady loading noise radiated at the second and fifth BPF harmonics is shown in Fig. 23 for an observer on the propeller disc orientated perpendicularly to the strut axis, i.e. at $[\theta_{\mathrm{exp}}, \phi_{\mathrm{exp}}] = [0, \pi/2]$. Data are computed for various strut configurations and are expressed in Pa to more clearly highlight changes in acoustic pressure as L varies. For $m = 2$, the pressure amplitude is maximum at the shortest propeller-strut distance and gradually decays for larger L until it reaches a plateau, suggesting that, when the strut is farther away, the noise emitted at this frequency may be dominated by the rotor steady loading and thickness noise. We observe a consistent trend across all cross-section diameters when the acoustic pressure is expressed as a function of the non-dimensional parameter L/D_s. Conversely, for $m = 5$, the sound level is considerably higher in the vicinity of the strut and decays exponentially with increasing distances, becoming negligible for $L/D_s > 3$. For instance, when represented on a decibel scale, the amplitude of the fifth harmonic for the D15 case exhibits an approximately linear decay with respect to the propeller-strut spacing, with an average slope of about $-1.1\,\mathrm{dB\,mm^{-1}}$ over the considered range. This outcome is consistent with the experimental findings of Gojon et al. [13] and aligns with the potential nature of the interaction under analysis.

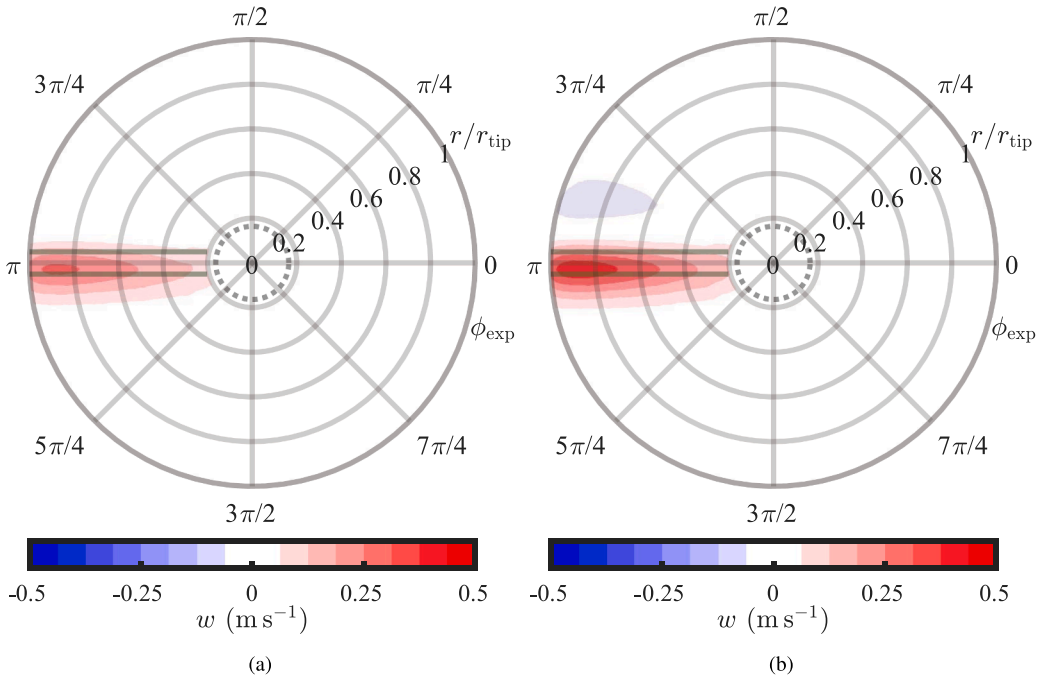

Fig. 20. Contours of the upwash velocity disturbance induced by the (a) D10 and (b) S10 struts at $L = 20\,\mathrm{mm}$. The propeller spins clockwise.

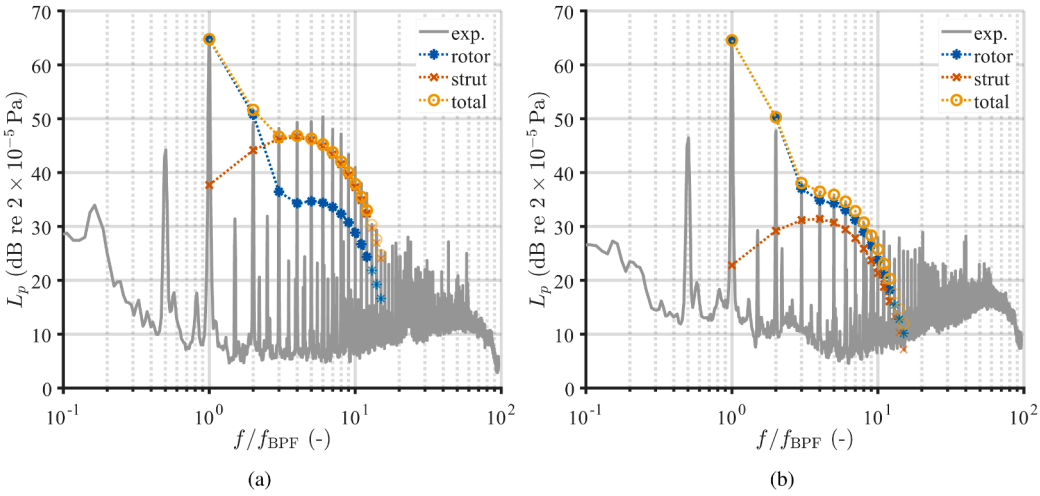

Fig. 21. Experimental spectra and predicted harmonics of the far-field noise radiated by the two-bladed propeller with the S10 strut at $L = 20\,\mathrm{mm}$ for (a) $[\theta_{exp}, \phi_{exp}] = [0, \pi/2]$ and (b) $[\theta_{exp}, \phi_{exp}] = [\pi/18, 0]$. The frequency axis is normalised by the BPF, whereas the transparent markers denote conditions for which the acoustic compactness assumption imposed in the analytical model is no longer valid.

Table 2
Parameters defining the investigated tapered circular cross-section struts. The strut diameters linearly vary from the root to the tip of the propeller. For each case, the strut axis is parallel to the rotor disc, implying that L remains constant.

Case #	Sketch	B (-)	L (m)	$D_{s,\mathrm{root}}$ (m)	$D_{s,\mathrm{tip}}$ (m)
1		2	0.02	0.01	0.02
2		2	0.02	0.02	0.01

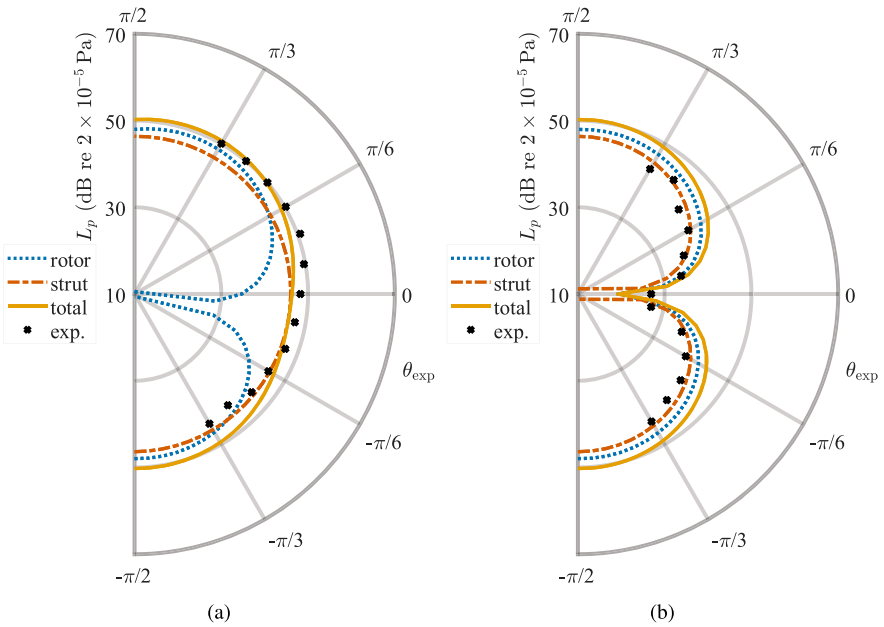

Fig. 22. Experimental and predicted directivity patterns of the far-field noise radiated at the fifth harmonic of the BPF by the two-bladed propeller with the S10 strut at $L = 20$ mm for (a) $\phi_{exp} = \pi/2$ and (b) $\phi_{exp} = 0$.

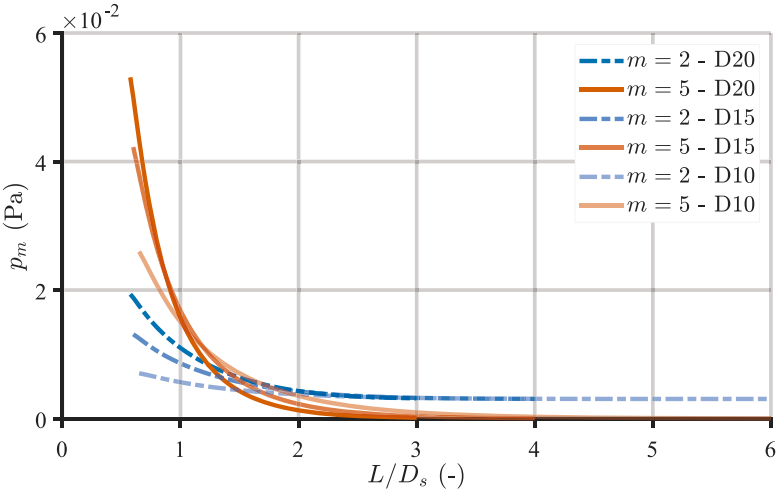

Fig. 23. Variation of the total far-field pressure over the normalised propeller-strut distance computed at the second and fifth BPF harmonics for $[\theta_{exp}, \phi_{exp}] = [0, \pi/2]$. The data refer to the two-bladed propeller and to struts with different circular cross-sections.

In view of the above, both the distance between the propeller and the strut and the blockage induced by the latter, which depends on its size, are key parameters that significantly influence the potential-interaction noise radiation. This insight can guide the design of supporting struts with cross-sections that change along the radius. As mentioned in Section 2, the strip approach used for discretising the blade and strut loads allows the parameters D_s and L to be expressed as functions of r. It is worth noting that the two-dimensional strip formulation presented in Section 2.3 for the strut loading noise neglects the influence of the potential field generated at other radii. This approximation is generally acceptable for straight cylinders but may become less accurate for tapered geometries, where the inboard contribution to the local potential field can be comparatively stronger. To mitigate this effect, we assume D_s and L to vary slowly with r.

With the goal of analysing the impact of a spanwise-varying cross-section on the noise emissions, we considered two reference cases of tapered struts, where the cross-section diameter changes progressively from the root to the tip of the propeller: one with D_s monotonically increasing from root to tip (Case 1) and the other with D_s monotonically decreasing from root to tip (Case 2). In both scenarios, the distance between the strut axis and the propeller disc remains constant. The geometrical parameters defining the

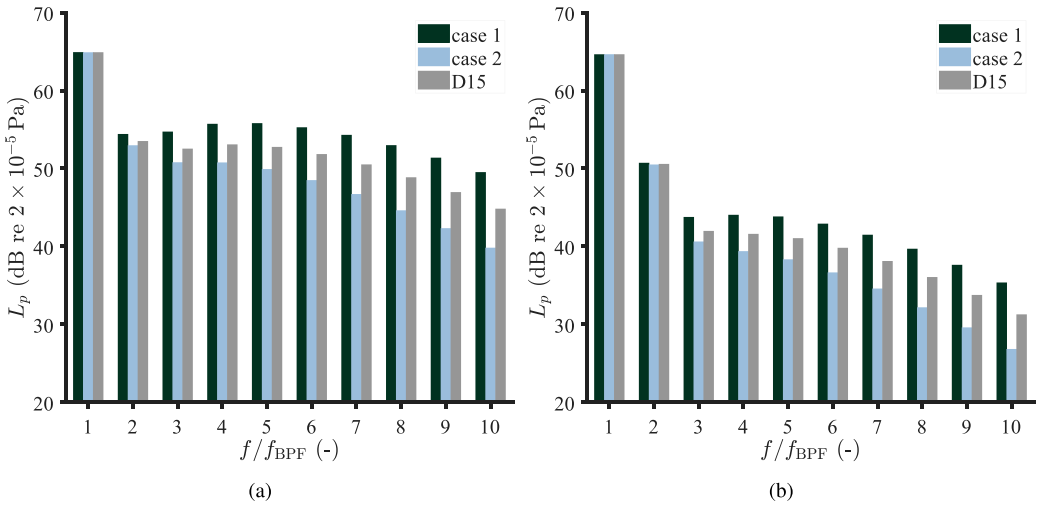

Fig. 24. Predicted harmonics of the total far-field noise radiated by the two-bladed propeller with the tapered circular cross-section struts outlined in Table 2 and the D15 strut for (a) $[\theta_{\mathrm{exp}}, \phi_{\mathrm{exp}}] = [0, \pi/2]$ and (b) $[\theta_{\mathrm{exp}}, \phi_{\mathrm{exp}}] = [\pi/18, 0]$. The frequency axis is normalised by the BPF.

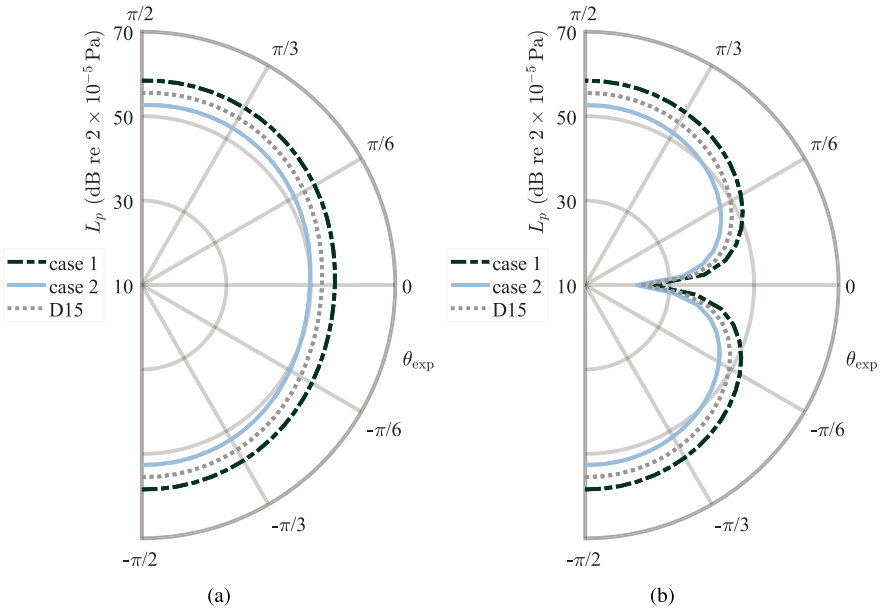

Fig. 25. Predicted directivity patterns of the far-field noise radiated at the fifth harmonic of the BPF by the two-bladed propeller with the tapered circular cross-section struts outlined in Table 2 and the D15 strut for (a) $\phi_{\mathrm{exp}} = \pi/2$ and (b) $\phi_{\mathrm{exp}} = 0$.

reference cases are listed in Table 2. It should be emphasised that these strut configurations are intended here as didactic examples and are not meant to represent realistic designs.

Fig. 24 shows the predicted BPF harmonics for the two-bladed propeller operating upstream of the two tapered struts. The reference case associated with the D15 strut, which features approximately the same surface area as the tapered configurations, is also included as a baseline for comparison purposes. The analysis focuses on two observers positioned normal to and in the vicinity of the strut axis. The sound pressure levels at the BPF are identical across all configurations, as they are dominated by rotor steady loading and thickness noise. In contrast, for both observer positions, the noise levels at higher harmonics display significant differences, with Case 2 being consistently quieter than Case 1. Notably, the ΔL_p between the two tapered cases increases with increasing frequencies, ranging from 1.4 dB at the second harmonic to 9.7 dB at the tenth harmonic for $\phi_{\mathrm{exp}} = \pi/2$ (Fig. 24a) and from 0.2 dB to 8.5 dB over the same range for $\phi_{\mathrm{exp}} = 0$ (Fig. 24b). The baseline configuration exhibits acoustic pressure levels that generally fall between those of the tapered designs throughout the frequency range. The maximum ΔL_p between the baseline and Case 2 is also found at high frequencies and reaches 5 dB and 4.4 dB at the tenth harmonic for $\phi_{\mathrm{exp}} = \pi/2$ and $\phi_{\mathrm{exp}} = 0$, respectively. Focusing on the fifth harmonic, the ΔL_p values remain nearly constant across all polar angles, as shown by the corresponding radiation patterns in Fig. 25. These results

demonstrate that local variations in strut geometry within the region of dominant sound generation can produce substantial changes in the radiated far-field noise.

5. Conclusion

This research work presents an analytical methodology to predict the potential-interaction tonal noise in a propeller-strut arrangement with minimal mathematical effort and low computational cost. Individual models describing blade loading noise, blade thickness noise, and strut loading noise are implemented and validated with an open-source database based on measurements from ISAE-SUPAERO. The aerodynamic sources and their sound radiation are modelled separately, with the former represented using potential flow solutions and the latter evaluated through Hanson's theory. In this framework, we propose a novel approach based on hypotrochoidal conformal mapping to describe the potential flow around polygons of various shapes, with the aim of predicting the unsteady loading sources generated by struts featuring non-circular cross-sections.

The model uses as input the spanwise distributions of the steady loads produced by an isolated propeller, which are assumed not to be affected by the presence of the strut and are estimated through an unsteady panel solver based on the surface vorticity method. The numerical results show reasonable agreement with the experimental static loads, exhibiting deviations of less than $8\,\%$ in thrust and $3\,\%$ in torque for a two-bladed propeller operating at $8000\,\mathrm{rpm}$. The discrepancy becomes more pronounced for higher numbers of blades, particularly in the case of the three-bladed propeller, suggesting that some physical mechanisms influencing the mean aerodynamics of the rotor are not fully encompassed by the mid-fidelity method. Nevertheless, despite its intrinsic limitations, this approach provides aerodynamic input data of sufficient accuracy for use within the noise prediction model while requiring only a fraction of the computational cost of higher-fidelity simulations. Such a trade-off makes it an attractive option for both industry and research applications.

We validate the analytical method against measurements for struts with different cross-section diameters and shapes, varying blade numbers, and multiple far-field observer locations. Overall, a satisfactory agreement is reached between the predictions and the experimental data for all BPF harmonics where the assumption of acoustic compactness remains valid, implying that the dominant physics of the propeller-strut potential interaction are correctly captured. For the two-bladed propeller, we estimate the sound pressure levels at the BPF, which are primarily governed by steady loading and thickness noise, with an accuracy within $1\,\mathrm{dB}$ across all directivity angles, confirming the suitability of our numerical approach for providing input data.

At higher harmonics, the model accurately reproduces the envelope shape of the frequency hump associated with potential interaction and estimates its level within $3\,\mathrm{dB}$ for most observer positions. More substantial deviations appear only at specific BPF harmonics or at polar angles far from the rotor disc. This may be attributed to secondary noise generation mechanisms that are not represented in the mathematical formulation, such as tip-vortex interaction or phase interference, with the latter being neglected since the rotor and strut contributions are summed incoherently. Moreover, the prediction results are found to be more accurate when the distortion is more significant, i.e. for larger strut diameters. In this regard, we can infer that, when the strut blockage reduces, the unsteady loading noise associated with the potential interaction contributes less to the overall noise. This allows other physical mechanisms of viscous nature, also neglected in the model, to become more relevant.

For propellers with a higher number of blades, the prediction accuracy decreases, particularly in the estimation of the unsteady loading noise from the strut, which appears to be more sensitive to the aerodynamic input. In addition, the assumption that the strut has a negligible effect on the aerodynamic performance of the propeller becomes less valid as the rotor solidity increases, leading to further underestimation of the steady loads. A more accurate numerical computation of the steady aerodynamic input of the rotor in the presence of the strut would be required in this case.

The analytical framework is then successfully applied to predict the potential interaction noise radiated by a propeller operating upstream of a square cross-section strut, thereby validating the use of the conformal-mapping approach. The results show that a square cross-section induces a stronger inflow distortion on the propeller disc than an equivalent circular cross-section of approximately the same size, thus affecting the associated unsteady loading noise. The methodology is not restricted to the specific mapping considered in this study but provides a general basis for reproducing a broad range of strut geometries and configurations. The possibility of prescribing arbitrary strut shapes opens novel opportunities for noise prediction models that have not yet been explored in the aeroacoustic community.

Finally, we demonstrate the capability of the proposed methodology to serve as an optimisation tool for UAV design through a parametric study assessing the influence of the strut-propeller distance on potential interaction noise. The sound produced by both the propeller and the strut due to unsteady loads is found to decay exponentially with increasing distances, becoming negligible for $L/D_s > 3$, in agreement with the literature. This finding has relevant implications for the design of struts with spanwise-varying cross-sections. Results from two tapered strut configurations, in which the cross-section diameter gradually changes from the blade root to the tip, show that a local variation in the strut geometry within the region of dominant noise sources, e.g. at $r/r_{\mathrm{tip}} \approx 0.8 - 0.9$, can lead to dramatic modifications in the radiated far-field noise. This application confirms that, despite its limitations and underlying assumptions, the proposed analytical approach can be effectively used to capture trends and variations in response to changes in input data, providing the level of accuracy required to identify minimum-noise UAV configurations in the early-stage design phase.

CRediT authorship contribution statement

R. Zamponi: Writing – original draft, Visualization, Validation, Software, Resources, Methodology, Investigation, Funding acquisition, Formal analysis, Data curation, Conceptualization; **A. Beni:** Writing – original draft, Visualization, Software, Formal analysis; **A.**

Zarri: Writing – review & editing, Supervision, Methodology; **J. Christophe:** Writing – review & editing, Visualization, Supervision, Software, Data curation.

Data availability statement

The data that support the findings of this study are available from the corresponding author upon reasonable request.

Declaration of competing interest

The authors declare that they have no known competing financial interests or personal relationships that could have appeared to influence the work reported in this paper.

Acknowledgments

The research presented in this paper has been funded by European Union's Horizon Europe Research and Innovation Programme under grant agreement No. 101138209 (eVTOLUTION). Views and opinions expressed are, however, those of the authors only and do not necessarily reflect those of the European Union or the European Climate, Infrastructure and Environment Executive Agency (CINEA). Neither the European Union nor the granting authority can be held responsible for them. In addition, the first author wishes to thank L.N.Z. for the fruitful discussions and valuable insight that contributed to the development of this work.

Appendix A. Conformal mapping parameters for various polygonal shapes

Table A.1
Parameters defining various polygonal shapes obtained using the hypotrochoidal mapping function with reference to the sketch in Fig. 4a. The dashed lines indicate the reference prescribed geometry, while the solid lines show the resulting hypotrochoidal curve.

Hypotrochoid	$N = R_d/R_r$ (-)	R_d/D_s (-)	ρ/R_r (-)	θ_0 (rad)
	2	0.75	0.33	$\pi/2$
	3	0.62	0.58	$7\pi/6$
	4	0.77	0.42	$\pi/4$	
	5	0.55	0.35	$\pi/2$

A set of polygonal shapes reproducible with the hypotrochoidal mapping function in Eq. (19), along with the parameters defining them, is given in Table A.1. Curves for N ranging from two to five are included. For each case, we specify the radius of the directing circle R_d and the offset ρ, which controls the smoothness of the corners, in order to reproduce a regular polygon with a side length of D_s, or, for the vertical ellipse, major and minor axes of D_s and $D_s/2$. These data are meant to offer an easy way to model the potential flow around struts with realistic cross-sections.

References

[1] National Academies of Sciences, Engineering, Medicine, Advancing Aerial Mobility: A National Blueprint, The National Academies Press, Washington, DC, 2020. https://doi.org/10.17226/25646

[2] M. Hassanalian, A. Abdelkefi, Classifications, applications, and design challenges of drones: a review, Prog. Aerosp. Sci. 91 (2017) 99–131. https://doi.org/10.1016/j.paerosci.2017.04.003

[3] S.A. Rizzi, D.L. Huff, D.D. Boyd, P. Bent, B.S. Henderson, K.A. Pascioni, D.C. Sargent, D.L. Josephson, M. Marsan, H.B. He, R. Snider, Urban Air Mobility Noise: Current Practice, Gaps, and Recommendations, Technical Report NASA/TP-2020-5007433, NASA Langley Research Center and NASA Glenn Research Center, 2020.

[4] M. Roger, E. Vella, J. Rendón, S. Moreau, Aerodynamic and sound-scattering effects in rotor-strut interaction noise of small-size drones, in: AIAA AVIATION Forum, American Institute of Aeronautics and Astronautics, San Diego, CA & Online, 2023. https://doi.org/10.2514/6.2023-4523
[5] J.E. Ffowcs Williams, D.L. Hawkings, Theory relating to the noise of rotating machinery, J. Sound Vib. 10 (1) (1969) 10–21. https://doi.org/10.1016/0022-460X(69)90125-4
[6] M. Roger, Aeroacoustic installation effects in propulsion systems, in: Measurement, Modelling and Simulations Techniques for Novel Aircraft Architectures, von Karman Institute for Fluid Dynamics, 2025. https://doi.org/10.35294/ls2025-01-roger
[7] C.E. Tinney, J. Sirohi, Multirotor drone noise at static thrust, AIAA J. 56 (7) (2018) 2816–2826. https://doi.org/10.2514/1.J056827
[8] H. Lee, D.-J. Lee, Rotor interactional effects on aerodynamic and noise characteristics of a small multirotor unmanned aerial vehicle, Phys. Fluids 32 (4) (2020) 047107. https://doi.org/10.1063/5.0003992
[9] R. Gojon, T. Jardin, H. Parisot-Dupuis, Experimental investigation of low Reynolds number rotor noise, J. Acoust. Soc. Am. 149 (6) (2021) 3813–3829. https://doi.org/10.1121/10.0005068
[10] M. Roger, D. Acevedo-Giraldo, M.C. Jacob, Acoustic versus aerodynamic installation effects on a generic propeller-driven flying architecture, Int. J. Aeroacoust. 21 (5-7) (2022) 585–609. https://doi.org/10.1177/1475472X221107372
[11] A. Zarri, E. Dell'Erba, W. Munters, C. Schram, Aeroacoustic installation effects in multi-rotorcraft: numerical investigations of a small-size drone model, Aerosp. Sci. Technol. 128 (2022) 107762. https://doi.org/10.1016/j.ast.2022.107762
[12] N.-S. Zawodny, D.-D. Boyd, Investigation of rotor-airframe interaction noise associated with small-scale rotary-wing unmanned aircraft systems, J. Am. Helicopter Soc. 65 (1) (2020) 1–17. https://doi.org/10.4050/JAHS.65.012007
[13] R. Gojon, H. Parisot-Dupuis, B. Mellot, T. Jardin, Aeroacoustic radiation of low Reynolds number rotors in interaction with beams, J. Acoust. Soc. Am. 154 (2) (2023) 1248–1260. https://doi.org/10.1121/10.0020672
[14] R. Gojon, T. Jardin, et al., Dataset corresponding to the publication : Aeroacoustic radiation of low Reynolds number rotors in interaction with beams, Gojon et al., JASA, 2023, 2025. https://doi.org/10.57745/MH70KE
[15] N. Doué, R. Gojon, T. Jardin, Numerical investigation of the acoustics radiation of a two-bladed rotor in interaction with a beam, in: Fluid-Structure-Sound Interactions and Control, Springer Nature Singapore, Singapore, 2024, pp. 169–176. https://doi.org/10.1007/978-981-97-6211-8_23
[16] M. Roger, K. Kucukcoskun, Near-and-far field modeling of advanced tail-rotor noise using source-mode expansions, J. Sound Vib. 453 (2019) 328–354. https://doi.org/10.1016/j.jsv.2019.02.007
[17] M. Roger, S. Moreau, Tonal-noise assessment of quadrotor-type UAV using source-mode expansions, Acoustics 2 (3) (2020) 674–690. https://doi.org/10.3390/acoustics2030036
[18] E. Cros, M. Roger, G. Serre, Low-frequency amplification of propeller tonal noise due to the scattering by a compact rigid cylinder, J. Sound Vib. 546 (2023) 117450. https://doi.org/10.1016/j.jsv.2022.117450
[19] J. Rendón-Arredondo, A. Arroyo Ramo, S. Moreau, M. Roger, A numerical and analytical approach of the sound-scattering effects in rotor-strut interaction noise of small-size drones, in: 30th AIAA/CEAS Aeroacoustics Conference, American Institute of Aeronautics and Astronautics, Rome, IT, 2024. https://doi.org/10.2514/6.2024-3047
[20] Y. Wu, M.J. Kingan, S.T. Go, Propeller-strut interaction tone noise, Phys. Fluids 34 (5) (2022) 055116. https://doi.org/10.1063/5.0090187
[21] A. Parry, D. Crighton, Prediction of counter-rotation propeller noise, in: 12th Aeroacoustic Conference, American Institute of Aeronautics and Astronautics, San Antonio, TX, 1989. https://doi.org/10.2514/6.1989-1141
[22] E. Vella, R. Gojon, H. Parisot-Dupuis, N. Doué, T. Jardin, M. Roger, Mutual interaction noise in rotor-beam configuration, AIAA J. (2026) 1–16. https://doi.org/10.2514/1.J065861
[23] J. Rendón-Arredondo, E. Vella, A. Arroyo Ramo, M. Roger, R. Gojon, T. Jardin, S. Moreau, Aeroacoustic investigations of a rotor-beam configuration in small-size drones, J. Acoust. Soc. Am. 158 (2) (2025) 1091–1102. https://doi.org/10.1121/10.0038975
[24] S.J. Kim, Y.-H. Hwang, R.S. Myong, H. Lee, Interactional aerodynamics and acoustics of a rotor with an airframe in hover, Phys. Fluids 36 (1) (2024) 017121. https://doi.org/10.1063/5.0185036
[25] R. He, M.J. Kingan, X. Wang, X. Kong, H. Zhu, Multi-rotor unmanned aerial vehicle rotor-strut interaction tonal noise, Appl. Acoust. 242 (2026) 111054. https://doi.org/10.1016/j.apacoust.2025.111054
[26] Z. Nehari, Conformal Mapping, McGraw–Hill, New York, 1952.
[27] S.A.L. Glegg, W.J. Devenport, Aeroacoustics of low mach number flows: fundamentals, analysis, and measurement, Academic Press, Amsterdam, 2nd edition, 2023.
[28] D.B. Hanson, D.J. Parzych, Theory for Noise of Propellers in Angular Inflow with Parametric Studies and Experimental Verification, Technical Report NAS 1.26:4499, NASA Glenn Research Center, 1993.
[29] M. Roger, S. Moreau, A. Guédel, Vortex-shedding noise and potential-interaction noise modeling by a reversed sears' problem, in: 12th AIAA/CEAS Aeroacoustics Conference, American Institute of Aeronautics and Astronautics, Cambridge, MA, 2006. https://doi.org/10.2514/6.2006-2607
[30] G.K. Batchelor, An Introduction to Fluid Dynamics, Cambridge Mathematical Library, Cambridge University Press, Cambridge, NY, 2000.
[31] W.R. Sears, Some aspects of non-stationary airfoil theory and its practical application, J. Aeronaut. Sci. 8 (3) (1941) 104–108. https://doi.org/10.2514/8.10655
[32] N.H. Kemp, W.R. Sears, Aerodynamic interference between moving blade rows, J. Aeronaut. Sci. 20 (9) (1953) 585–597. https://doi.org/10.2514/8.2758
[33] T. Theodorsen, General Theory of Aerodynamic Instability and the Mechanism of Flutter, Technical Report NACA-TR-496, NACA, 1935.
[34] D.B. Hanson, Noise of counter-rotation propellers, J. Aircraft 22 (7) (1985) 609–617. https://doi.org/10.2514/3.45173
[35] L.M. Milne-Thomson, Theoretical Hydrodynamics, Macmillan Press, London, 5th edition, 1979.
[36] D.T. Solanki, D.S. Sharma, Potential flow around polygonal shaped cylinders using hypotrochoidal mapping function, Int. J. Mech. Sci. 226 (2022) 107395. https://doi.org/10.1016/j.ijmecsci.2022.107395
[37] R. Zamponi, S. Moreau, C. Schram, Rapid distortion theory of turbulent flow around a porous cylinder, J. Fluid Mech. 915 (2021) A27. https://doi.org/10/gjb3f8
[38] L. Crawshaw, A. Karimian, C.C. Paruchuri, A.B. Parry, S. Palleja-Cabre, E. Arcondoulis, Reduction of propeller-strut interaction noise by porosity, in: 30th AIAA/CEAS Aeroacoustics Conference, American Institute of Aeronautics and Astronautics, Rome, IT, 2024. https://doi.org/10.2514/6.2024-3386
[39] P.J. Baddoo, L.J. Ayton, Potential flow through a cascade of aerofoils: direct and inverse problems, Proc. R. Soc. A 474 (2217) (2018) 20180065. https://doi.org/10.1098/rspa.2018.0065
[40] P.J. Baddoo, Lightning solvers for potential flows, Fluids 5 (4) (2020) 227. https://doi.org/10.3390/fluids5040227
[41] R.K. Amiet, Acoustic radiation from an airfoil in a turbulent stream, J. Sound Vib. 41 (4) (1975) 407–420. https://doi.org/10.1016/S0022-460X(75)80105-2
[42] V. Ahuja, R.J. Hartfield, Aerodynamic loads over arbitrary bodies by method of integrated circulation, J. Aircraft 53 (6) (2016) 1719–1730. https://doi.org/10.2514/1.C033619
[43] W.O. Valarezo, V.D. Chin, Method for the prediction of wing maximum lift, J. Aircraft 31 (1) (1994) 103–109. https://doi.org/10.2514/3.46461
[44] L.F. Richardson, The approximate arithmetical solution by finite differences of physical problems involving differential equations, with an application to the stresses in a masonry dam, Philos. Trans. R. Soc. Lond. A 210 (459–470) (1911) 307–357. https://doi.org/10.1098/rsta.1911.0009
[45] D.V. Shenoy, R. Gojon, T. Jardin, M.C. Jacob, Aerodynamic and acoustic study of a small scale lightly loaded hovering rotor using large eddy simulation, Aerosp. Sci. Technol. 150 (2024) 109219. https://doi.org/10.1016/j.ast.2024.109219
[46] F. Fortin, V. Ahuja, Comparison of aerodynamic loads for a rotor in hover using two surface-vorticity approaches, in: AIAA SCITECH Forum, American Institute of Aeronautics and Astronautics, Orlando, FL, 2024. https://doi.org/10.2514/6.2024-0005
[47] Y. Jo, T. Jardin, R. Gojon, M.C. Jacob, J.-M. Moschetta, Prediction of noise from low reynolds number rotors with different number of blades using a non-linear vortex lattice method, in: 25th AIAA/CEAS Aeroacoustics Conference, American Institute of Aeronautics and Astronautics, Delft, NL, 2019. https://doi.org/10.2514/6.2019-2615